J. Fluid Mech. (2020), *vol*. 899, A32. © The Author(s), 2020.
Published by Cambridge University Press
doi:10.1017/jfm.2020.430

The interactions of rectangular synthetic jets with a laminar cross-flow

Lei Wang[1] **and Li-Hao Feng**[1],†

[1]Fluid Mechanics Key Laboratory of Education Ministry, Beijing University of Aeronautics and Astronautics, Beijing 100191, PR China

(Received 4 October 2019; revised 19 March 2020; accepted 23 May 2020)

Three-dimensional flow fields of a rectangular synthetic jet with aspect ratio of 3 and its interaction with a laminar cross-flow are measured using time-resolved tomographic particle image velocimetry. The synthetic-jet to free-stream velocity ratio is fixed at 1, and two orifice orientations, normal to (spanwise configuration) and aligned with (streamwise configuration) the cross-flow direction, respectively, are investigated. The flow scenarios are composed of a tilted vortex ring, a secondary trailing vortex and a tertiary near-wall vortex. Compared to previous results for circular cases, the legs of the trailing structures are found to be jointed in the spanwise direction by two shear-layer vortices at different wall-normal heights. In addition, the near-wall vortex is a crescent-shaped spanwise vortex. For the first time, as the peculiar process of non-circular vortex rings in quiescent condition, axis switching is validated to exist in the cross-flow. Associated with axis switching, the spanwise case exhibits interaction between the leeward vortex of the vortex ring and the downstream shear-layer vortex, which causes slower penetration and recovery of vortex ring tilting, but faster jet transition. Furthermore, the trailing structures and vortex ring are weakened, leading to lower peaks of the velocity deficit and overshoot in the jet region than those for the streamwise case. On the other hand, the spanwise case can induce a stronger near-wall vortex, which transfers more momentum and initial disturbance into the boundary layer. Consequently, the spanwise case yields larger velocity gradient and velocity fluctuation peak inside the boundary layer with a lower shape factor, suggesting greater efficiency of promoting boundary-layer transition.

Key words: boundary layer control, vortex dynamics, jets

1. Introduction

The manipulation and optimization of jets have always attracted attention in the field of flow control. According to different external conditions, the major investigations of jets can be divided into two broad categories: jets in quiescent condition (i.e. free jets) and jets in cross-flow (JICF). Compared to free jets, JICF complicate the flow-field features by interaction with the cross-flow. As documented in extensive research, the flow field of a circular steady jet issued into a cross-flow can form a complex set of vortical structures, including counter-rotating vortex pairs, windward and leeward shear-layer vortices, upstream horseshoe vortices and upright wake vortices (Margason 1993; Fric

† Email address for correspondence: lhfeng@buaa.edu.cn

https://doi.org/10.1017/jfm.2020.430 Published online by Cambridge University Press

& Roshko 1994; Kelso, Lim & Perry 1996). Based on the relevant flow physics, JICF are better at entrainment and mixing than free jets (Mahesh 2013), and therefore are widely used in engineering and environmental control systems, such as fuel injection in gas-turbine combustors, film cooling of turbine blades, thrust vector control of high-speed vehicles, industrial mixing and pollutant dispersion (Smith & Mungal 1998; New, Lim & Luo 2003; Mahesh 2013).

The trend towards lower energy consumption in aerodynamics has promoted active or passive flow control techniques to further improve the control efficiency of jets. Synthetic jets (Smith & Glezer 1998; Glezer & Amitay 2002) are effective in actively controlling vortex generation through periodically oscillating the fluid in a working system. Holman *et al*. (2005) studied the formation criteria for synthetic jets, namely that the reciprocal of the Strouhal number must be larger than 0.16 and 1 for circular and two-dimensional (2-D) synthetic jets, respectively. On that condition, a strong synthetic jet can form trains of discrete vortical structures, which transfer momentum into the external environment to modify aerodynamic shape (DeMauro, Leong & Amitay 2013; Feng & Wang 2014), or to delay or suppress flow separation (Zhang & Zhong 2011; Tang *et al.* 2014).

For synthetic jets in quiescent condition, two main dimensionless parameters, Reynolds number (Re) and dimensionless stroke length (L), are used to determine the flow state of vortical structures, and their motion distance from the jet exit in one cycle, respectively. Research on circular or 2-D synthetic jets has manifested increased near-field entrainment and spreading rates in comparison with steady jets (Cater & Soria 2002; Smith & Swift 2003). With the merits of compact size and low cost of manufacture, synthetic jets in cross-flow have shown potential applications in the flow control community. A series of studies have been implemented to reveal the flow physics.

Crook & Wood (2001) studied a cylinder with an array of circular synthetic jets in a cross-flow. The results showed tilting and stretching of vortex rings. In addition, a well-defined streamwise vortex pair was observed immediately downstream of each jet orifice to interact with the separated flow. Zhong, Millet & Wood (2005) utilized dye flow visualization to investigate the behaviour of circular synthetic jets with Re_L (based on stroke length) from 16 to 245, L from 0.56 to 1.4 in a laminar boundary layer at velocity ratio (VR) from 0.06 to 0.7. The vortical structures exhibited three types with increased L and VR: hairpin vortices, stretched vortex rings, and tilted and distorted vortex rings. As a continuous work, Jabbal & Zhong (2008) established the dimensionless parameter space of the above three vortical structures. They found an upper limit of $\mathrm{VR} = 0.4$ for both hairpin vortices and stretched vortex rings, the thermal footprints of which produced two streaks of high surface heat transfer downstream of the orifice. Conversely, only a single streak of high surface heat transfer could be observed for tilted and distorted vortex rings. Similar to the flow pattern of the 2-D circular cylinder model in Crook & Wood (2001), either hairpin vortices or stretched vortex rings could be responsible for delaying flow separation.

To understand the underlying flow mechanism, Zhou & Zhong (2009) and Jabbal & Zhong (2010) used three-dimensional (3-D) numerical simulation and 2-D particle image velocimetry (PIV) to study the flow fields of the above three vortical structures. Hairpin vortices and stretched vortex rings exhibited the characteristics of a streamwise vortex pair embedded in the boundary layer with a common upwash, while tilted and distorted vortex rings induced a tertiary streamwise vortex pair in the near-wall region with a common downwash. By measuring the wall shear stress, stretched vortex rings were found to offer the best performance of higher near-wall fluid mixing, persistency and lower spatial fluctuations. Other works have focused on the operation condition, e.g. actuator location

https://doi.org/10.1017/jfm.2020.430 Published online by Cambridge University Press

and frequency of circular (Lardeau & Leschziner 2011; Zhang & Zhong 2011) and 2-D slot (Dandois, Garnier & Sagaut 2007) synthetic jets on reducing the size of the separated region for a turbulent boundary layer separating from a ramp.

Recently, flow control with synthetic jets from non-circular orifices has been popular due to their enhanced entrainment and mixing compared to circular and 2-D synthetic jets. The main mechanism can be attributed to axis switching of non-circular vortex rings, i.e. the major axis and minor axis of vortex rings are interchanged relative to their initial orientations due to azimuthal non-uniform shear-layer curvature (Gutmark & Grinstein 1999; Grinstein 2001). Rectangular configurations are of particular interest by virtue of their wide applications in aviation and industry. Based on the orifice aspect ratio (AR), the investigations of rectangular synthetic jets involve two classes: high aspect ratio ($\mathrm{AR} > 5$) and low aspect ratio ($\mathrm{AR} \leq 5$). The works of Amitay & Cannelle (2006), Kotapati, Mittal & Cattafesta (2007), Van Buren, Whalen & Amitay (2014) and Van Buren & Amitay (2016) can provide sufficient understanding of the flow structures and flow-field characteristics for high-AR rectangular synthetic jets in quiescent condition.

In terms of interaction with a cross-flow, Smith (2002) carried out a wind-tunnel experiment of an $\mathrm{AR} = 45$ rectangular synthetic jet actuator array in a turbulent boundary layer at $\mathrm{VR} = 1.2$. He examined two orifice orientations, with the rectangular long side normal to and aligned with the cross-flow direction, respectively. The boundary layer of the former developed a wake-like region due to the blockage effect, while the latter formed streamwise vortices embedded within the boundary layer. However, it is difficult to understand how the flow structures influence the boundary layer from the measurements by hot-wire anemometry. Ravi, Mittal & Najjar (2004) focused on interactions of square, and $\mathrm{AR} = 2$ and 4 rectangular synthetic jets with a cross-flow using 3-D numerical simulations; however, the details on the evolution of vortical structures cannot be obtained from the limited results. Van Buren *et al.* (2016*a*) used stereoscopic PIV to study $\mathrm{AR} = 6$, 12 and 18 rectangular synthetic jets normally issued into a laminar boundary layer at $\mathrm{VR} = 0.5$, 1 and 1.5. The flow fields were characterized by a recirculation region downstream of the orifice and a steady streamwise vortex pair farther downstream, akin to the findings in Smith (2002). In addition, the virtual blockage of the jet was reduced with the decreased AR. In another similar study, Van Buren *et al.* (2016*b*) investigated the orifice orientation with pitch ($20°-90°$) and skew ($0°-90°$) angles on the vortex formation of an $\mathrm{AR} = 18$ rectangular orifice. Three types of scenarios, i.e. no coherent vortices, a singular strong streamwise vortex or a symmetric streamwise vortex pair, were detected for different combinations of the orifice skew and pitch angles. The orifice with larger pitch and smaller skew angles caused higher blockage, and thus a stronger velocity deficit in the free stream.

From the above, the flow structures for rectangular synthetic jets in cross-flow exhibit some differences from those for circular ones, suggesting an important role of the orifice configuration in flow control effectiveness. Most of the existing studies pertain to high-AR ($\mathrm{AR} > 5$) synthetic jets; however, the interactions of low-AR ($\mathrm{AR} \leq 5$) ones with a cross-flow have rarely been reported. The recent works of Wang *et al.* (2018), Shi, Feng & Wang (2019) and Wang, Feng & Xu (2019) have demonstrated significant entrainment and mixing enhancement for low-AR non-circular synthetic jets in quiescent condition associated with axis switching and streamwise vortices. Therefore, low-AR rectangular synthetic jets in cross-flow are worth studying in detail to achieve better flow control applications.

https://doi.org/10.1017/jfm.2020.430 Published online by Cambridge University Press

This paper aims to explore the fundamental interactions between low-AR rectangular synthetic jets and a cross-flow. The focus is to analyse the impact of the orifice orientation on the evolution of the flow structures and the relevant flow physics. For this purpose, two different orifice orientations relative to the cross-flow direction were investigated for an AR = 3 rectangular orifice. Note that this aspect ratio was selected considering that AR = 3 displayed superior entrainment performance for rectangular free synthetic jets with ARs from 1 to 5 (Wang *et al*. 2018). In addition, tomographic PIV measurement was performed to characterize the flow field three-dimensionality. It is hoped that the current results are helpful for understanding the mechanism by which low-AR non-circular synthetic jets influence control.

2. Experimental set-up and methodology

2.1. *Experimental facility*

The experiments were conducted in a recirculation water tunnel (Zhu *et al*. 2017) with a Plexiglas test section of 3000 mm (length) × 700 mm (width) × 600 mm (height). The maximum free-stream velocity in the test section could be up to 0.5 m s^{-1} with the turbulence level no more than 0.8 %. The synthetic jet actuator in this investigation was a piston-type one, as shown by the dashed box in figure 1(*a*). The length of the connecting rod was $l_c = 300$ mm, and the diameter of the piston was $D_p = 29$ mm. The synthetic jet actuator was connected with an L-shaped hollow circular cylinder to horizontally generate synthetic jets underwater. Note that the horizontal section of the L-shaped cylinder was 100 mm, and that was long enough to avoid the impact of the bent part on the formation of synthetic jets. A detailed introduction to this synthetic jet device could be found in Feng & Wang (2010) and Xu *et al.* (2018). The end of the L-shaped cylinder was flush-mounted in a plate with the jet orifice. The plate was mounted vertically to the bottom of the test section, and the cross-flow direction was parallel to the plate surface.

During the experiments, the water height was kept at 550 mm, and the temperature was 26 ± 0.2 °C. The plate was made of anodized aluminium with 1500 mm (length) × 500 mm (width) × 10 mm (thickness), and this gave a blockage ratio of approximately 1.3 %. The leading edge of the plate was modified to be a 1 : 5 elliptic shape to minimize flow separation and boundary-layer transition. Two AR = 3 rectangular configurations with different orientations were investigated in this study. The rectangular long side was normal to, and aligned with, the free-stream direction, namely spanwise and streamwise configurations, respectively (figure 1*b*). The circular equivalent diameter of the orifice was $D_e = 8$ mm. The position of the jet orifice was 700 mm ($87.5D_e$) away from the leading edge of the plate. The plate surface was 400 mm ($50D_e$) away from the sidewall of the test section, which could guarantee less wall influence on the investigated field in the wall-normal direction. The coordinate system was defined such that the origin was located at the centre of the jet orifice with the x-axis along the free-stream direction, y-axis normal to the plate and z-axis along the spanwise direction.

2.2. *Synthetic jet and cross-flow parameters*

Throughout the experiments, the servo electromotor of the synthetic jet actuator was controlled by a constant sinusoidal wave signal, and the excitation frequency and amplitude of the synthetic jet actuator were fixed at $f_e = 2$ Hz (the excitation cycle $T = 1/f_e = 0.5$ s) and $A_e = 1.38$ mm. The circular equivalent diameter was used as the characteristic length by referring to the previous non-circular jet study (Gutmark &

https://doi.org/10.1017/jfm.2020.430 Published online by Cambridge University Press

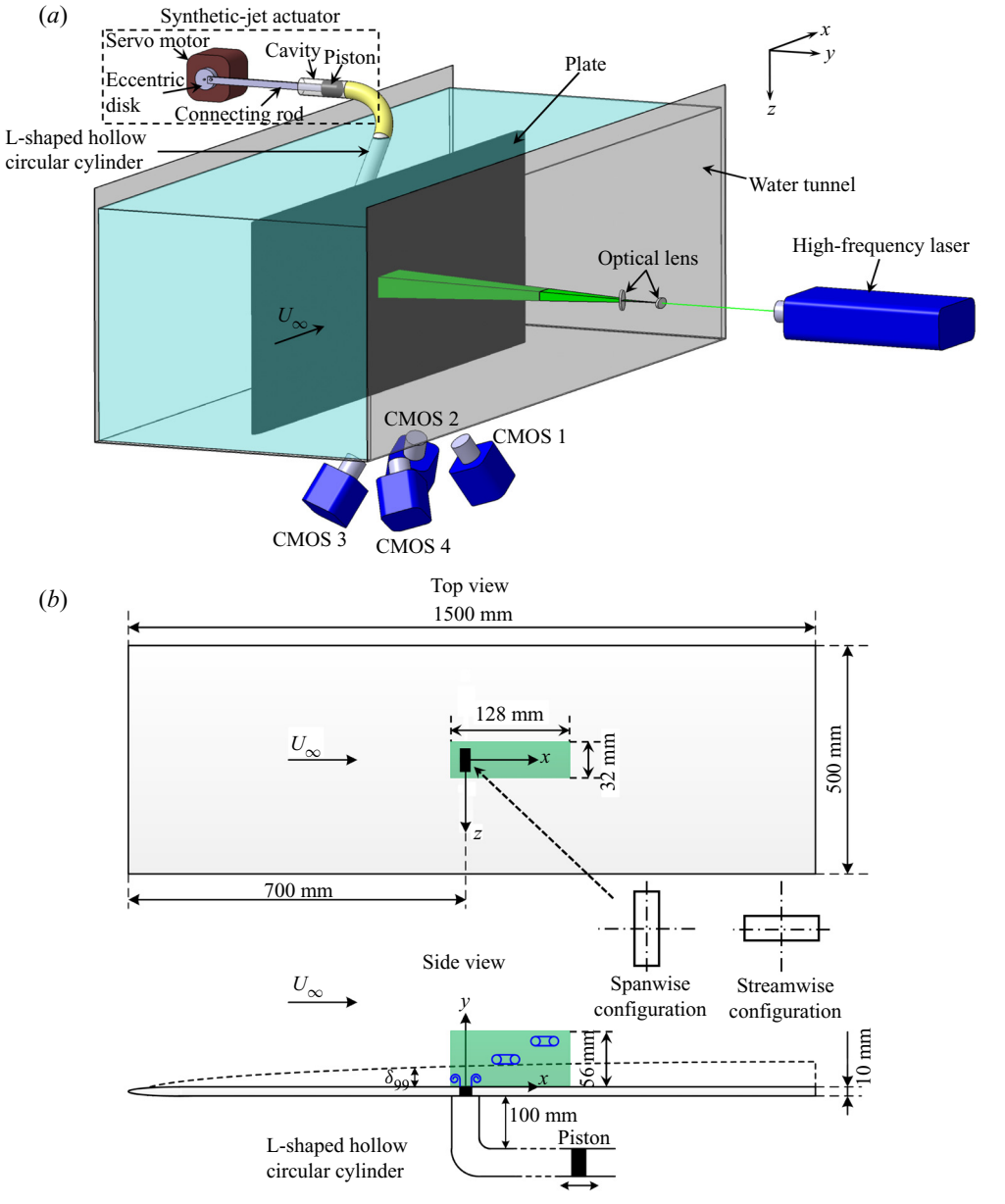


FIGURE 1. (*a*) Isometric schematic view of experimental set-up for tomographic PIV in the test section of the water tunnel. (*b*) Top and side views of the plate in (*a*), and spanwise and streamwise configurations of the AR = 3 rectangular orifice.

Grinstein 1999). The instantaneous velocity at the jet exit $u(t)$ can be simplified as follows based on mass conservation of the incompressible flow when $l_c \gg A_e$ ($A_e/l_c = 0.0046$):

$$u(t) \approx 2\pi A_e f_e (D_p/D_e)^2 \sin(2\pi f_e t). \tag{2.1}$$

https://doi.org/10.1017/jfm.2020.430 Published online by Cambridge University Press

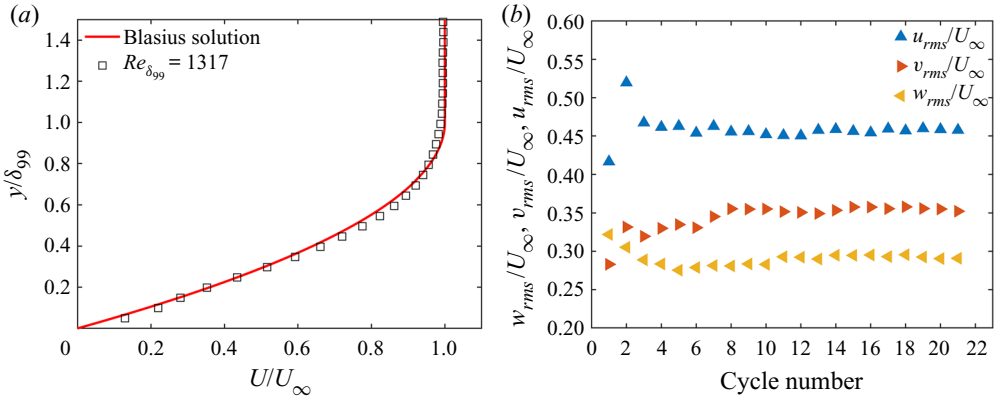


FIGURE 2. (*a*) Comparison of undisturbed boundary-layer velocity profile at the jet exit with the theoretical Blasius solution. (*b*) Normalized velocity fluctuations u_{rms}/U_∞, v_{rms}/U_∞ and w_{rms}/U_∞ at the vortex core near the jet exit versus cycle number for the spanwise case.

The averaged velocity at the jet exit U_0 is expressed as follows (Smith & Glezer 1998; Glezer & Amitay 2002), i.e. the time-averaged blowing velocity over the entire cycle:

$$U_0 = \frac{1}{T}\int_0^{T/2} u(t)\,\mathrm{d}t = 2A_e f_e (D_p/D_e)^2. \tag{2.2}$$

Thus $U_0 = 72.5$ mm s^{-1}, and the two main dimensionless parameters of the synthetic jet, Reynolds number was $Re_{U_0} = 664$ and dimensionless stroke length was $L = 4.5$, defined as

$$Re_{U_0} = U_0 D_e/\nu, \tag{2.3}$$

$$L = L_0/D_e = U_0 T/D_e, \tag{2.4}$$

where ν is the kinematic viscosity of water, and L_0 is the stroke length.

The free-stream velocity over the plate in the test section was $U_\infty = 71.3 \pm 0.8$ mm s^{-1}, and thus the synthetic-jet to free-stream velocity ratio VR $= U_0/U_\infty \approx 1$. This velocity ratio was used so as to compare the current results with previous studies for high-AR rectangular synthetic jets (Van Buren *et al.* 2016*a*,*b*) under the same velocity ratio. Near the wall, the maximum streamwise velocity fluctuation upstream of the orifice did not exceed 4 % of the free-stream velocity, indicating the current noise level. The boundary-layer thickness δ_{99} at the jet exit was 16.12 mm ($2.02D_e$) determined by 99 % U_∞ corresponding to the free-stream Reynolds number of $Re_{\delta_{99}} = 1317$. The boundary-layer shape factor is computed as

$$H = \frac{\delta^*}{\theta} = \frac{\int_0^\infty \left(1 - \frac{U_x}{U_\infty}\right)\mathrm{d}y}{\int_0^\infty \frac{U_x}{U_\infty}\left(1 - \frac{U_x}{U_\infty}\right)\mathrm{d}y}, \tag{2.5}$$

where δ^* and θ denote the displacement thickness and the momentum thickness, respectively. At the jet exit, H was 2.60, indicating the laminar flow regime in the boundary layer. The comparison of the undisturbed velocity profile at the jet exit with the theoretical Blasius solution is shown in figure 2(*a*). Relevant parameters of the synthetic jet and boundary layer are summarized in table 1.

https://doi.org/10.1017/jfm.2020.430 Published online by Cambridge University Press

Synthetic jet	U_0 (mm s^{-1})	D_e (mm)	Re_{U_0}	L	AR	VR
	72.5	8	664	4.5	3	1
Boundary layer	U_∞ (mm s^{-1})	δ_{99} (mm)	$Re_{\delta_{99}}$	δ^* (mm)	θ (mm)	H
	71.3	16.12	1317	5.00	1.93	2.60

TABLE 1. Major parameters of synthetic jet and boundary layer at the jet exit.

2.3. *Tomographic particle image velocimetry measurements*

Time-resolved tomographic PIV was applied to measure the 3-D velocity fields of rectangular synthetic jets interacting with a cross-flow (figure 1*a*). For comparison, the 3-D velocity field of a rectangular synthetic jet issued into a quiescent environment was also measured; and note that the y-axis corresponds to the streamwise direction for the free case. Hollow glass beads with diameters in the range of 5–20 μm and density of 1.05 g cm^{-3} were seeded to a particle image density of 0.05 particles per pixel. A high-frequency double-pulsed solid-state laser (Vlite-Hi-30k, 532 nm wavelength, 2×30 mJ pulse^{-1} at 1 kHz) was used to produce the volumetric illumination source perpendicular to the plate through a combination of two optical lenses. The width of the volumetric illumination source and its location relative to the orifice centre in the x-axis direction were adjusted according to the cases with and without cross-flow.

Four high-speed complementary metal oxide semiconductor (CMOS) cameras (Photron Fastcam SA2/86K-M3) equipped with 85 mm Nikon lenses at $f/11$ were distributed under the bottom of the test section to capture the particle images in the investigated field (figure 1*a*). The viewing angle between CMOS 1 and CMOS 4 (CMOS 2 and CMOS 3) was approximately 60°, and that between CMOS 1 and CMOS 2 (CMOS 3 and CMOS 4) was approximately 30°. The distance between the lens and the measurement domain was around 700 mm, corresponding to a focus depth of 40 mm, guaranteeing the recording of all the particles in the measurement volume in focus. Before the experiment, the cameras, laser and data acquisition system were accurately synchronized by a synchronous controller. Each camera resolution was set to 2048 (x) × 1024 (y) pixels for the cases in cross-flow, and to 1024 (x) × 2048 (y) pixels for the free case.

The sequences of particle images were captured at 1 kHz ($\Delta t = 0.001$ s). A pair of particle images with the interval of $3\Delta t$ was used to calculate each velocity vector field. By doing this, the maximum particle displacement between adjacent frames was less than 10 pixels. In total, 10 914 particle images were recorded after the jet flow was adequately steady. To save calculation time, 50 instantaneous velocity fields were reserved in each excitation cycle, and thus the actual time resolution was 100 Hz (50 times the excitation frequency), which could effectively resolve the vortex dynamics. Using the spanwise configuration as an example, we performed a convergence examination of the velocity fluctuations at the vortex core near the jet exit (figure 2*b*). The results showed that the variation level of all the velocity fluctuations was less than 1 % of the free-stream velocity after the cycle number of 8. This result could meet the current comparable analysis of the flow fields of different orifice orientations.

In image preprocessing, after background subtraction and Gaussian smoothing with a grid size of 3×3 pixels, volume self-calibration was implemented to improve the accuracy of the mapping function (Wieneke 2008) to achieve the reduction of the original disparity error to less than 0.1 pixel. Using the self-calibrated mapping function, the 3-D

https://doi.org/10.1017/jfm.2020.430 Published online by Cambridge University Press

particle intensity distribution was reconstructed following the MART algorithm (Elsinga *et al.* 2006). The measurement volume size was 128 mm (x) × 56 mm (y) × 32 mm (z) ($16D_e \times 7D_e \times 4D_e$) for the cases in cross-flow (figure 1*b*), and 60 mm (x) × 104 mm (y) × 32 mm (z) ($7.5D_e \times 13D_e \times 4D_e$) for the free case, respectively. The digital image resolution was 14.3 pixels mm^{-1} corresponding to the resolution of 13.2 voxels mm^{-1} in the object space. The 3-D vector field was calculated by an iterative cross-correlation algorithm with multi-grid and window deformation (Scarano & Riethmuller 2000), and the final interrogation volume size was 48 × 48 × 48 voxels with 75 % overlap. Then the space resolution was 3.64 mm ($0.46D_e$) and the vector spacing was 0.91 mm ($0.11D_e$) in each direction, enabling the large-scale vortical structures to be resolved in this study. The resulting 3-D vector field was spatially filtered using a divergence-free smoothing algorithm (Wang *et al.* 2016).

The experimental uncertainty is mainly attributed to the entire data size and the cross-correlation analysis of PIV. Specifically, the uncertainties in the mean velocity and velocity fluctuation can be estimated as (Ye, Schrijer & Scarano 2016)

$$\varepsilon_u = \frac{\sigma_u}{\sqrt{N}}, \tag{2.6}$$

$$\varepsilon_{u_{rms}} = \frac{\sigma_u}{\sqrt{2(N-1)}}, \tag{2.7}$$

where σ_u is the typical level of normalized streamwise velocity fluctuations, and N is the number of uncorrelated samples. In this study, the maximum of the normalized streamwise velocity fluctuation is less than 0.6, corresponding to the maximum of ε_u and $\varepsilon_{u_{rms}}$ being 2 % and 1 %, respectively. In addition, an error of 0.2 pixel is considered for the cross-correlation algorithm (Elsinga *et al.* 2006); the resulting velocity uncertainty is 2 % relative to the jet maximum velocity.

2.4. *Data analysis methods*

This section gives a brief outline of the methods applied in this study, including the vortex centre detection, the finite-time Lyapunov exponent and the Fourier mode decomposition.

2.4.1. *Vortex centre detection*

In the quantitative analysis of vortex dynamics, the vortex centre location (x_v, y_v, z_v) is defined as the centroid of the vorticity (Cantwell & Coles 1983) as

$$x_v = \frac{1}{\Gamma}\int_{\Omega} x\omega \,\mathrm{d}\Omega, \tag{2.8}$$

$$y_v = \frac{1}{\Gamma}\int_{\Omega} y\omega \,\mathrm{d}\Omega, \tag{2.9}$$

$$z_v = \frac{1}{\Gamma}\int_{\Omega} z\omega \,\mathrm{d}\Omega, \tag{2.10}$$

$$\Gamma = \int_{\Omega} \omega \,\mathrm{d}\Omega, \tag{2.11}$$

where Ω is the vortex region. To determine the vortex region, the λ_{ci} criterion is first used to identify vortices, which is defined as the imaginary part of the complex

https://doi.org/10.1017/jfm.2020.430 Published online by Cambridge University Press

eigenvalue of the velocity gradient tensor (Zhou *et al.* 1999). Here the velocity gradient tensor is computed using the finite difference scheme with second-order accuracy. Sensitivity analysis has been conducted to examine the vortical structures with the λ_{ci} thresholds of 1 to 3.5 s^{-1} with 0.5 s^{-1} increment. The flow area with a λ_{ci} above 1.5 s^{-1} is recognized as the vortex area, which can display global characteristics of the 3-D vortical structures clearly. In addition, the main structures have no obvious change as λ_{ci} increases from 1.5 to 3.5 s^{-1}, and thus a larger λ_{ci} of 3.5 s^{-1} is also used concurrently to characterize the main components in this study. Within the vortex area, the above integrations are calculated for the phase-averaged vorticity satisfying $|\omega|/|\omega_p| \geq 0.1$ (here ω_p denotes the local vorticity peak) to eliminate noise from the PIV data (Feng & Wang 2010; Xu *et al.* 2018). Based on sensitivity analysis, by selecting normalized vorticity levels of 0.05 to 0.2 with 0.05 increment, the circulation of the vortex ring is insensitive to this cut-off level with the difference less than 3 %.

2.4.2. *Finite-time Lyapunov exponent*

The λ_{ci} criterion can effectively identify large-scale vortical structures. However, as vortices break into small scales in the downstream propagation, the results with a smaller threshold of λ_{ci} could be contaminated by noise in the data, leading to a hard observation. The identification of Lagrangian coherent structures (LCSs) provides a robust method to deal with this issue, which can be achieved through computing the finite-time Lyapunov exponent (FTLE) field (Haller & Yuan 2000; Shadden, Dabiri & Marsden 2006).

For a time-dependent flow map $\boldsymbol{\phi}_{t_0}^{t_0+T_F}(\boldsymbol{x}_0) : \boldsymbol{x}(t_0) \mapsto \boldsymbol{x}(t_0 + T_F)$ that maps fluid particles from their initial position $(\boldsymbol{x}_0, t_0)$ to their later position over a finite time T_F, the Cauchy–Green strain tensor is expressed as (Haller 2015)

$$\boldsymbol{C}_{t_0}^{t_0+T_F}(\boldsymbol{x}_0) = [\nabla \boldsymbol{\phi}_{t_0}^{t_0+T_F}(\boldsymbol{x}_0)]^{\mathrm{T}} \nabla \boldsymbol{\phi}_{t_0}^{t_0+T_F}(\boldsymbol{x}_0), \tag{2.12}$$

and the FTLE can be computed as (Green, Rowley & Haller 2007; Xu *et al.* 2018)

$$\mathrm{FTLE}_{T_F}(\boldsymbol{x}_0, t_0) = \ln \sqrt{\lambda_{max}(\boldsymbol{C}_{t_0}^{t_0+T_F}(\boldsymbol{x}_0))}/|T_F|, \tag{2.13}$$

where $\lambda_{max}(\boldsymbol{C}_{t_0}^{t_0+T_F}(\boldsymbol{x}_0))$ represents the largest singular value of $\boldsymbol{C}_{t_0}^{t_0+T_F}(\boldsymbol{x}_0)$. The LCSs are indicated by ridges in the FTLE field corresponding to the regions of maximum fluid particle separation ($T_F > 0$) or attraction ($T_F < 0$). The ridge in the forward-time ($T_F > 0$) FTLE field represents a repelling LCS, and that in the backward-time ($T_F < 0$) FTLE field represents an attracting LCS. In this study, the 3-D FTLE is computed on a Cartesian grid with a resolution of 0.2 mm × 0.2 mm × 0.2 mm ($0.025D_e \times 0.025D_e \times 0.025D_e$) over a backward-time integration of $T_F = -1.5$ s, equal to three times the jet cycle ($T = 0.5$ s). This integration time enables one to identify details of the flow structures in the far-downstream field considering acceptable computational expense. The numerical integration adopts a fourth-order Runge–Kutta method with a time step of 0.01 s, and the space grid is interpolated by trilinear interpolation.

2.4.3. *Fourier mode decomposition*

Fourier mode decomposition (FMD) is a useful tool to extract important dynamical information from the complex flow (Ma *et al.* 2015; Qu *et al.* 2017). The FMD can decompose the flow field into a train of modes corresponding to the coherent structures with a specific frequency based on discrete Fourier transformation (DFT) of the data at

https://doi.org/10.1017/jfm.2020.430 Published online by Cambridge University Press

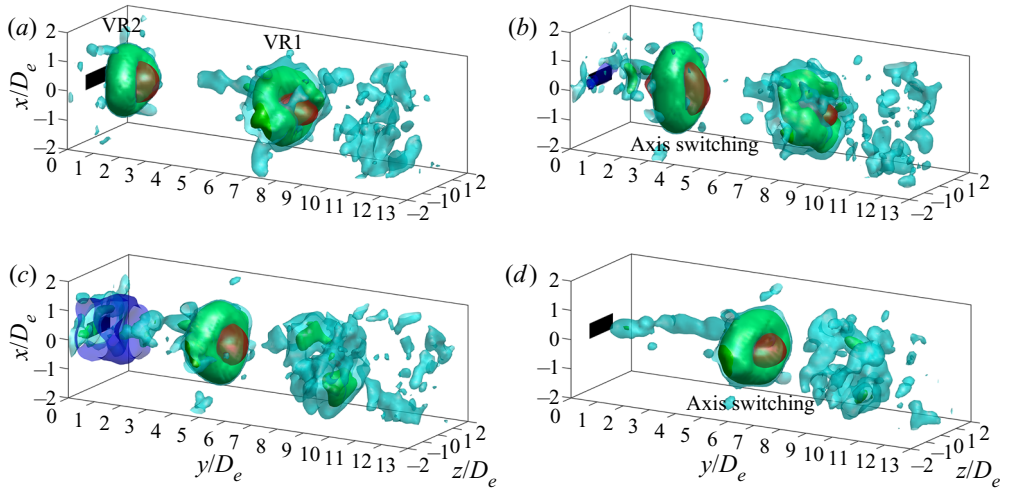


FIGURE 3. Temporal evolution of the AR = 3 rectangular free synthetic jet at $t/T = 0.25$ (*a*), 0.5 (*b*), 0.75 (*c*) and 1 (*d*). Isosurfaces of phase-averaged $\lambda_{ci} = 1.5$ (cyan) and 3.5 (green), and jet velocity $u_y/U_\infty = 1$ (red) and -0.1 (blue, near the jet exit during the suction period) are presented. VR denotes vortex ring, and 1 and 2 denote the vortical structures from two consecutive cycles.

each sampling point. When dealing with a quasi-periodic flow, the FMD has similarity in the global power spectrum, and the spatial modes corresponding to the characteristic frequencies with the dynamic mode decomposition method. However, the FMD has fewer limitations in the original data dimension and consumes less calculation time, and thus could be appropriate for the 3-D flow-field decomposition. One can refer to the work of Ma *et al*. (2015) for more details of the FMD algorithm. In this study, FMD is used to extract dynamical information from the boundary-layer flow to reveal the impact of the jet.

3. Rectangular synthetic jet in quiescent environment

This section focuses on the characteristics of an AR = 3 rectangular synthetic jet issued into a quiescent environment, which can provide the basis for understanding the complex interactions with the cross-flow. Figure 3 shows the temporal evolution of the phase-averaged field for the AR = 3 rectangular synthetic jet. Vortical structures are visualized by isosurfaces of λ_{ci}, and those corresponding to two typical thresholds of $\lambda_{ci} = 1.5$ (cyan) and 3.5 (green) are displayed together, which could help to distinguish the flow structures with different scales and strengths.

Synthetic jet vortex rings (VR1 and VR2) from two consecutive cycles are observed in the investigated field. Owing to azimuthal non-uniformity of the shear-layer growth rate (Gutmark & Grinstein 1999), the VR2 immediately initiates self-induced deformation from the jet exit. Such self-induced deformation results in subsequent interchange of the major axis and minor axis of the vortex ring relative to the initial orientations, indicating the first axis switching. With axis switching, the jet velocity with the VR2 exhibits compression and stretching in the initial major-axis and minor-axis directions, respectively (see $u_y/U_\infty = 1$ in figure 3*b*).

It is noticed that, at the maximum suction moment, the synthetic jet produces evident reverse flow at the jet exit (see $u_y/U_\infty = -0.1$ in figure 3*c*). That has little effect on the

https://doi.org/10.1017/jfm.2020.430 Published online by Cambridge University Press

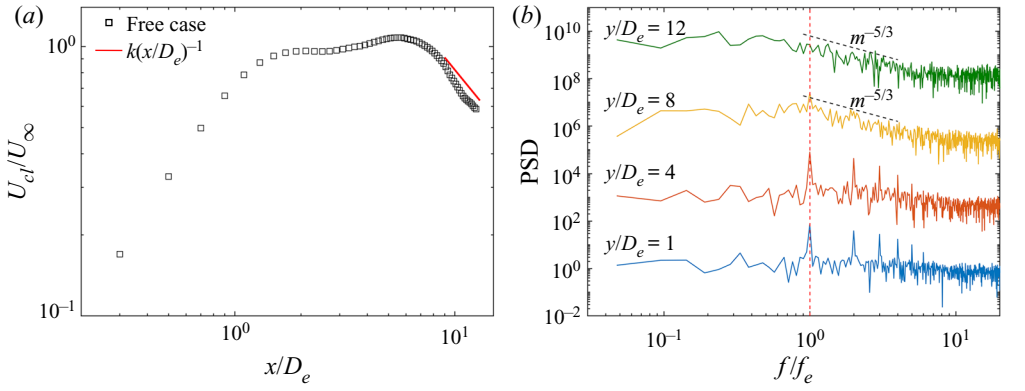


FIGURE 4. (*a*) Streamwise variation of jet centreline velocity U_{cl}/U_∞. (*b*) Power spectral density (PSD) of jet centreline velocity at $y/D_e = 1$, 4, 8 and 12. Each power spectrum has been shifted upward by 10^3 relative to the former one.

VR2, which has moved far away from the jet exit. Then the VR2 undergoes the second axis switching, and interchanges its major axis and minor axis again. The jet velocity exhibits opposite variation to that during the first axis switching (figure 3*d*). After that, the vortex ring becomes more distorted through developing azimuthal instability (Nichols, Schmid & Riley 2007), and eventually breaks into small scales, as reflected by the evolution of the VR1.

Figure 4 presents the streamwise variation of the time-averaged jet centreline velocity and the related power spectrum to reflect the flow-field characteristics. After reaching the maximum, the downstream behaviour ($x/D_e > 9$) of the jet centreline velocity asymptotically approaches an $(x/D_e)^{-1}$ decay law, suggesting the tendency of the rectangular synthetic jet towards an axisymmetric turbulent jet. In the power spectra, profound peaks corresponding to the excitation frequency and its high harmonics are observed at $y/D_e = 1$ and 4 since the near flow field ($x/D_e < 6$) of the synthetic jet is dominated by periodic motion of vortex rings. As the vortical structures break down, the peak of the dominant frequency is gradually reduced, and has disappeared at $y/D_e = 12$. Concurrently, the local slope is close to the Kolmogorov scaling of $-5/3$, reflecting the flow transition to a turbulent one.

4. Vortical evolution in cross-flow

4.1. *Identification of vortical structures*

Figures 5 and 6 present the temporal evolution of the phase-averaged fields for the spanwise and streamwise cases, respectively. The vortical structures are visualized by isosurfaces of λ_{ci} like those in the quiescent condition. In addition, the vertical velocity $u_y/U_\infty = 0.4$ (red) and -0.04 (blue) is also shown to reflect the local induced velocities of different vortical structures. Owing to the similar components of the vortical structures for the two cases, we give a representative description mainly based on the spanwise case.

As shown in figure 5, the vortical structures for rectangular synthetic jets in cross-flow are composed of a tilted vortex ring (TVR) followed by a secondary trailing vortex (STV). The TVR exhibits downstream tilting, associated with the trailing structures, which establish an obstacle to the cross-flow and inhibit the momentum injection

https://doi.org/10.1017/jfm.2020.430 Published online by Cambridge University Press

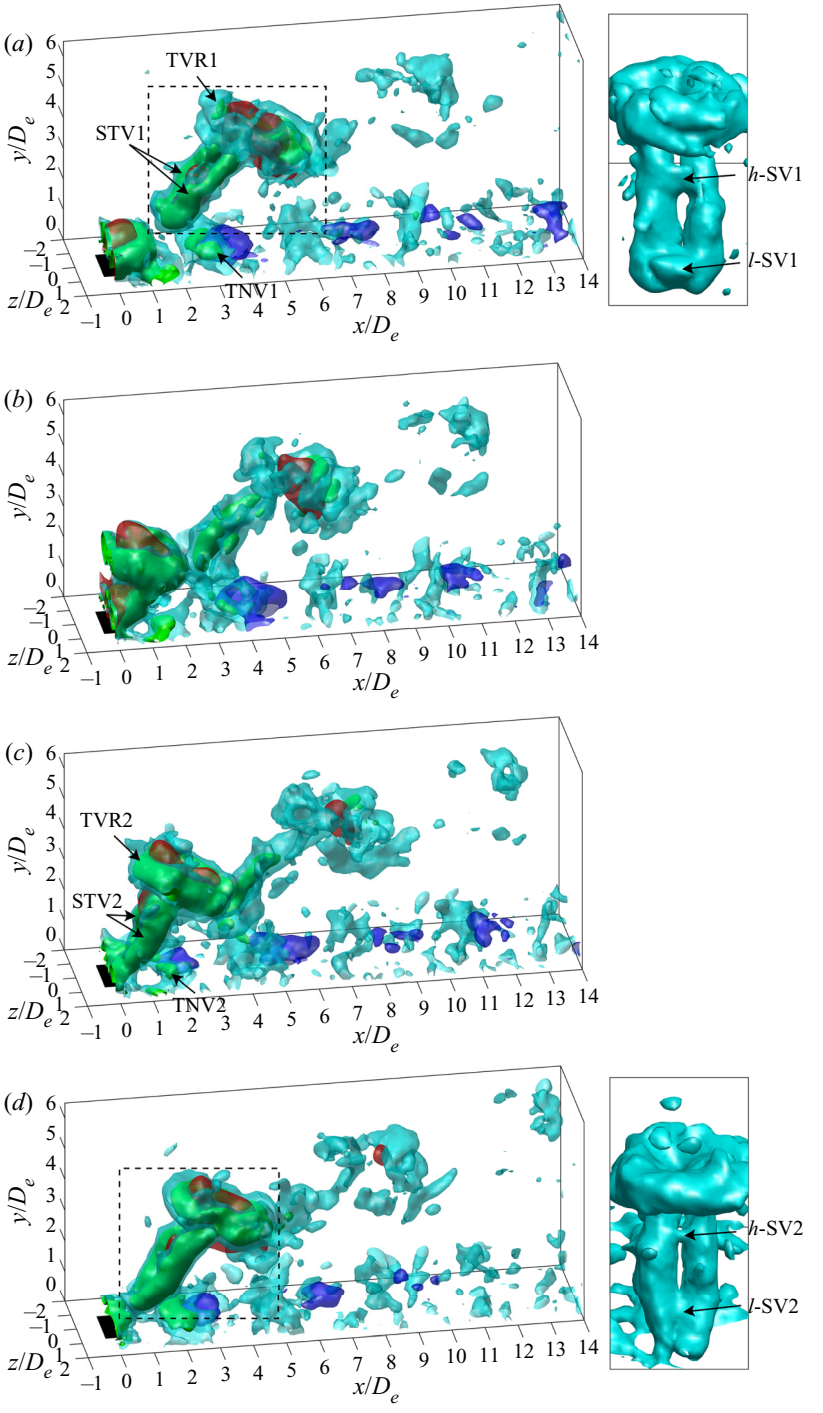


FIGURE 5. Temporal evolution of the spanwise case at $t/T = 0.25$ (*a*), 0.5 (*b*), 0.75 (*c*) and 1 (*d*). Isosurfaces of phase-averaged $\lambda_{ci} = 1.5$ (cyan) and 3.5 (green), and vertical velocity $u_y/U_\infty = 0.4$ (red) and -0.04 (blue, in the downstream near-wall region) are presented. Front views zooming-in on the black dashed box are shown on the right of (*a*) and (*d*). TVR, STV and TNV denote tilted vortex ring, secondary trailing vortex and tertiary near-wall vortex; *h*-SV and *l*-SV denote higher and lower shear-layer vortices, respectively.

https://doi.org/10.1017/jfm.2020.430 Published online by Cambridge University Press

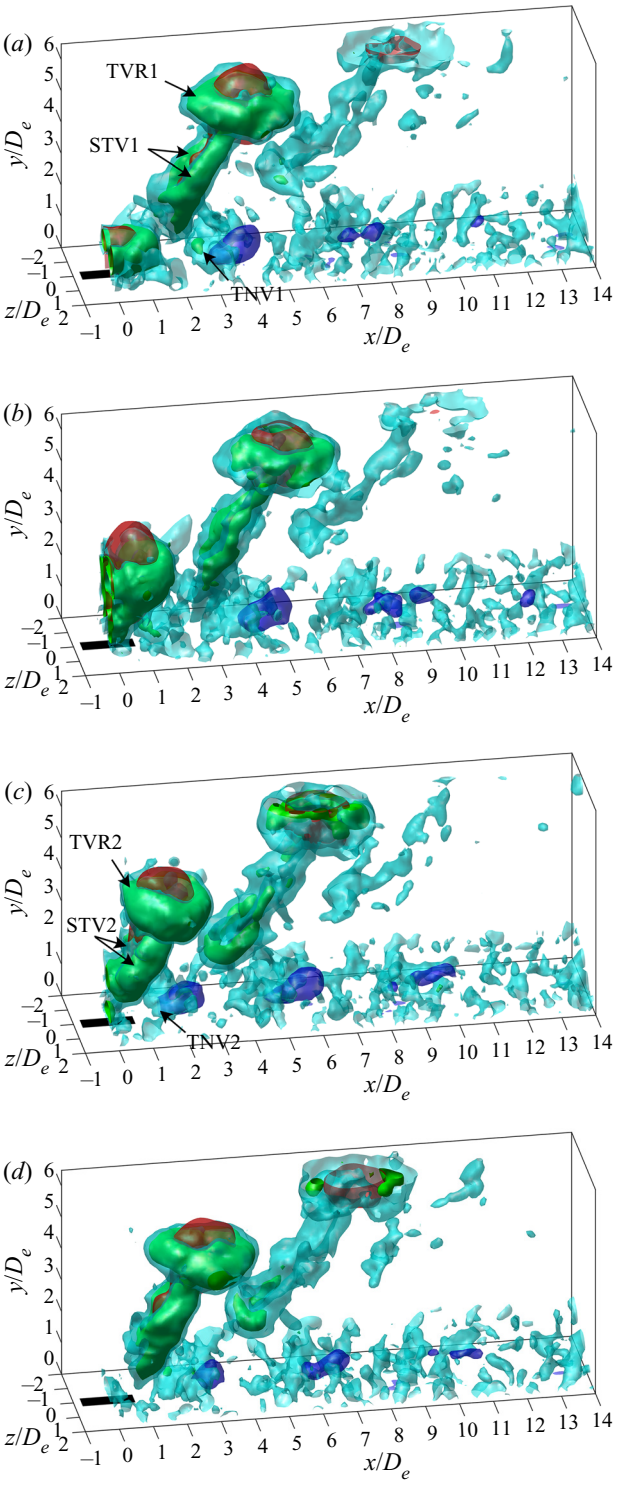


FIGURE 6. Temporal evolution of the streamwise case at $t/T = 0.25$ (*a*), 0.5 (*b*), 0.75 (*c*) and 1 (*d*). Identical isosurfaces with those in figure 5 are presented.

https://doi.org/10.1017/jfm.2020.430 Published online by Cambridge University Press

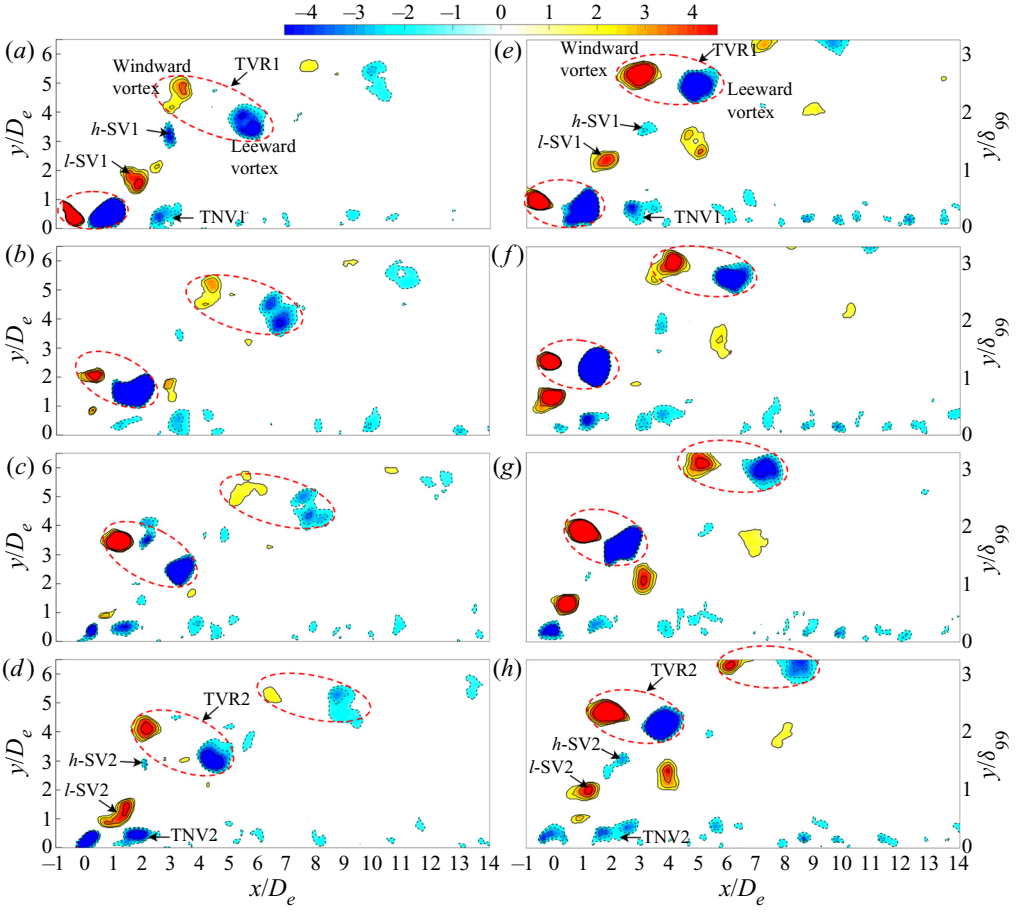


FIGURE 7. Contours of $\lambda_{ci}\omega_z/|\omega_z|$ ($\lambda_{ci} \geq 1.5$) in the jet symmetry plane for the (*a–d*) spanwise and (*e–h*) streamwise cases at $t/T = 0.25$ (*a*,*e*), 0.5 (*b*,*f*), 0.75 (*c*,*g*) and 1 (*d*,*h*). The upstream and downstream vortices inside the red dashed ellipse denote the windward and leeward vortices of the TVR. Solid and dashed lines represent positive and negative values, respectively. Contour levels are ± 1.

into the downstream branch of the vortex ring. In contrast, the upstream branch has higher momentum, and thus a larger propagation velocity than the downstream one. Consequently, the jet column as well as the vortex ring becomes bent downstream in the cross-flow direction, consistent with the results for pulse jets (Sau & Mahesh 2008) and plasma synthetic jets (Zong & Kotsonis 2019) in cross-flow.

The STV is essentially a pair of counter-rotating vortices branching from the middle of the vortex ring. It has the same rotation sense as the corresponding longitudinal edge of the vortex ring. As a result, an upwash velocity is induced between the two legs of the STV, and inside the vortex ring (see $u_y/U_\infty = 0.4$). This upwash velocity can lift the low-momentum fluid away from the wall, leading to the local velocity deficit in the lee side of the jet. It is interesting to find that the STV does not extend to the wall, whereas the ends of the two legs are jointed in the spanwise direction by a shear-layer vortex named *l*-SV. Over the *l*-SV, another shear-layer vortex is detected to be seated on the STV underneath the upstream branch of the TVR, namely *h*-SV (see the zoom-in in figure 5*a*,*d*). These two

https://doi.org/10.1017/jfm.2020.430 Published online by Cambridge University Press

shear-layer vortices will be further depicted in figure 7. In addition, a tertiary near-wall vortex (TNV) in a crescent shape is formed near the wall due to induction of the STV and *l*-SV. The TNV convects with a downwash velocity induced on its downstream side (see $u_y/U_\infty = -0.04$). This downwash velocity can be advantageous for momentum injection near the wall.

The current flow scenarios exhibit vortex rings that convect downstream and penetrate the boundary layer ($\delta_{99} \approx 2D_e$). These features have also been observed in the numerical results of Ravi *et al.* (2004) for rectangular synthetic jets with ARs of 1, 2 and 4 in cross-flow. The difference is that their vortices penetrated out of the boundary layer with a longer streamwise distance due to the relatively low VR of 0.5. However, the vortex rings were not formed in previous studies of high-AR (AR > 5) rectangular synthetic jets in cross-flow (Van Buren *et al.* 2016*a*,*b*). In addition, some differences in the vortical structures can be found in comparison with the tilted and distorted vortex rings for circular synthetic jets (Jabbal & Zhong 2010), which are summarized as follows: the legs of the present STV are connected in the spanwise direction by the two shear-layer vortices at different wall-normal heights, and the present TNV is a crescent-shaped spanwise vortex rather than a longitudinal streamwise vortex pair as in Jabbal & Zhong (2010).

Contours of $\lambda_{ci}\omega_z/|\omega_z|$ ($\lambda_{ci} \geq 1.5$) in the jet symmetry plane for the two cases are compared in figure 7. The red dashed ellipse surrounding the windward and leeward vortices of the TVR can reflect the tilting angle. As the vortical structures move away from the wall, the TVR is gradually recovered to the wall-parallel orientation associated with the Biot–Savart induced effect under the cross-flow. As the STV becomes weak and breaks downstream, its inhibition to the cross-flow is diminished. According to the Kutta–Joukowski theorem, the windward vortex of the vortex ring experiences a downward force, while the leeward vortex experiences an upward force, leading to upstream tilting of the vortex ring (Sau & Mahesh 2008). In particular, the vortex ring for the streamwise case exhibits faster recovery of the tilting angle and penetration through the boundary layer.

In addition, the shear-layer vortices are detected in the jet symmetry plane for the two cases that have a clockwise rotation for the *h*-SV, and an anticlockwise rotation for the *l*-SV. The *l*-SV is generated by the shear layer rolling-up in the windward side of the initial jet. However, the *h*-SV evidently differs from the *l*-SV, and has not been identified in previous research. It is inferred that the *h*-SV is resulted from the shear between high-momentum, outer cross-flow and low-momentum, near-wall fluid lifted by the STV, akin to the formation mechanism of the secondary and tertiary hairpin vortices in Zhou & Zhong (2010).

4.2. *Axis switching in cross-flow*

Axis switching of vortex rings is a crucial mechanism for non-circular jets in quiescent condition, by which they can significantly enhance entrainment and mixing relative to comparable circular and 2-D jets (Gutmark & Grinstein 1999; Grinstein 2001). However, for steady jets in cross-flow, axis switching no longer happens to non-circular orifices since the presence of a counter-rotating vortex pair inhibits the formation of the vortex ring (Lim, New & Luo 2001; New *et al.* 2003). For synthetic jets in cross-flow, vortex rings revert to primary structures as the form of stretched or tilted vortex rings. Hence, whether vortex rings can experience axis switching is of practical interest for non-circular synthetic jets in cross-flow. To our knowledge, no existing research has reported this.

The variation of the vortex ring diameter in the characteristic plane can reflect axis switching of vortex rings, which is defined as the distance between vortex centres corresponding to the positive and negative vorticities. Further, the vortex ring centre is

https://doi.org/10.1017/jfm.2020.430 Published online by Cambridge University Press

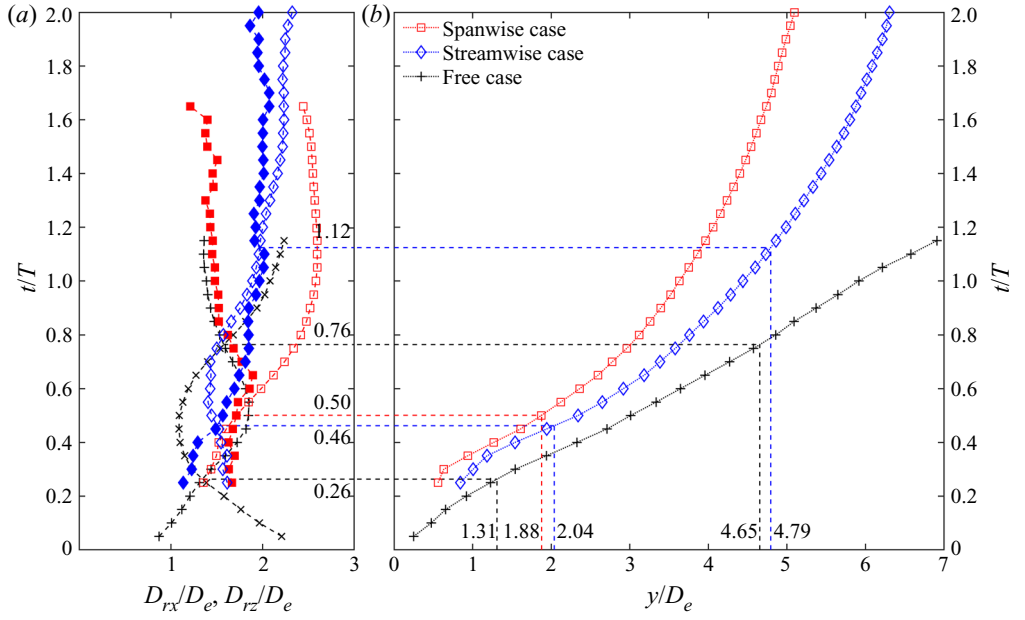


FIGURE 8. (*a*) Temporal evolution of vortex ring diameters D_{rx}/D_e and D_{rz}/D_e: D_{rx} (—+—) and D_{rz} (—×—) denote the vortex ring diameters in the *y*–*x* and *y*–*z* planes for the free case; D_{rx} (—□—, spanwise case; —◇—, streamwise case) and D_{rz} (—■—, spanwise case; —◆—, streamwise case) denote the vortex ring diameters in the *x*–*y* plane, and the plane through the vortex ring centre and normal to the vortex ring tilting plane. (*b*) Trajectory of vortex ring centre along the wall-normal direction for the three cases.

obtained from the middle of the vortex ring diameter in the jet symmetry plane. Figure 8 shows the temporal evolution of the vortex ring diameter and vortex ring centre for the two cases, and the result for the free case is presented for comparison. For the vortex area identified by $\lambda_{ci} = 1.5\ \mathrm{s}^{-1}$, the uncertainty of the vortex ring diameter is approximately 5 %. In addition, the influence of the vortex area on the vortex ring diameter has also been analysed by selecting the λ_{ci} thresholds of 0.5 to 2 s^{-1} with 0.5 s^{-1} increment. The variation of the vortex area is found to have little effect on the vortex ring diameter, and the difference of the present result could be within 5 %.

The diameter curves for the free case have two intersection points corresponding to two axis switchings. It is worth noting that the intersection also exists for the spanwise and streamwise cases, respectively, suggesting that the present rectangular synthetic jets in cross-flow can experience axis switching of vortex rings. This is an important difference between non-circular synthetic jets and steady jets in cross-flow. Specifically, the spanwise case undergoes once, while the streamwise case undergoes twice. In addition, the spanwise case has the latest first axis switching ($t/T = 0.50$), whereas the location ($y/D_e = 1.88$) is lower than that of the streamwise case ($y/D_e = 2.04$) due to slower vortex penetration (figure 8*b*).

Axis switching for the three cases can be intuitively displayed by the vortex filament through the vortex centre, as shown in figure 9. For the free case, the cylindrical coordinate system (r, θ, y) is used to determine the vortex centre location (r_v, y_v) in the radial plane by changing θ by 3° increments. The entire vortex centre locations are connected by a spline curve to obtain the vortex filament. For the case in cross-flow, rotation and translation

https://doi.org/10.1017/jfm.2020.430 Published online by Cambridge University Press

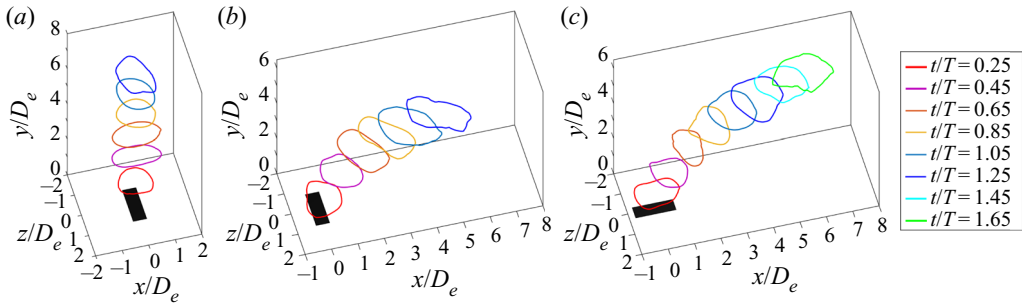


FIGURE 9. Temporal evolution of vortex filament through vortex centre for the (*a*) free, (*b*) spanwise and (*c*) streamwise cases, respectively.

of the coordinate are performed firstly to keep the vortex ring axisymmetric about the y-axis through the origin. Then the same method as the above is used to obtain the vortex filament, which is finally restored to the original spatial location.

Compared to self-induced deformation for the free case, the vortex deformation for the spanwise and streamwise cases can be affected by the cross-flow. Owing to the obstacle of the trailing structures to the cross-flow near the wall, the upstream section of the vortex filament is mainly affected by the cross-flow relative to the downstream one. For the spanwise case, the cross-flow has opposite direction to the azimuthal induced velocity of the upstream section, resulting in an unfavourable effect on the local vortex deformation. Conversely, the downstream section yields relatively larger streamwise stretching (see $t/T = 0.25$ in figure 9*b*). As the vortex filament moves away from the wall, the impact of the cross-flow on the downstream section increases. As a result, the vortex filament is evidently stretched in the streamwise direction after the first axis switching (see $t/T = 1.25$ in figure 9*b*), which can also be reflected by the vortex ring diameter in the jet symmetry plane (figure 8*a*). Hence, no new axis switching follows.

On the contrary, the initial azimuthal induced velocity of the upstream section has the same direction as the cross-flow for the streamwise case, leading to a favourable effect on the local vortex deformation. Consequently, the streamwise case has an earlier first axis switching than the spanwise case as depicted in figure 8. Additionally, the streamwise case has slower streamwise stretching under the cross-flow, and therefore the vortex filament can experience two axis switchings like the free case.

4.3. *Vortex interactions*

Owing to the periodic property of synthetic jets, interactions between different vortical structures are important for synthetic jets in cross-flow. The FTLE enables one to effectively identify the details of vortical evolution in the far-downstream field. Figure 10 exhibits contours of the backward-time FTLE in the jet symmetry plane for the two cases. The leeward vortex of the TVR is observed to interact with the downstream l-SV for the spanwise case. They approach each other and become a pair of contour-rotating vortices. Then the l-SV is entrained by the leeward vortex into the TVR as the vortical structures propagate downstream, as marked by white dashed circles in figure 10(*a*,*b*). However, such a process does not happen to the streamwise case, where the leeward vortex moves away from the l-SV with vortex penetration.

The schematics in figure 11 can aid 3-D illustration of the difference between the two cases. Compared to the independent TVR and STV for the streamwise case, the spanwise

https://doi.org/10.1017/jfm.2020.430 Published online by Cambridge University Press

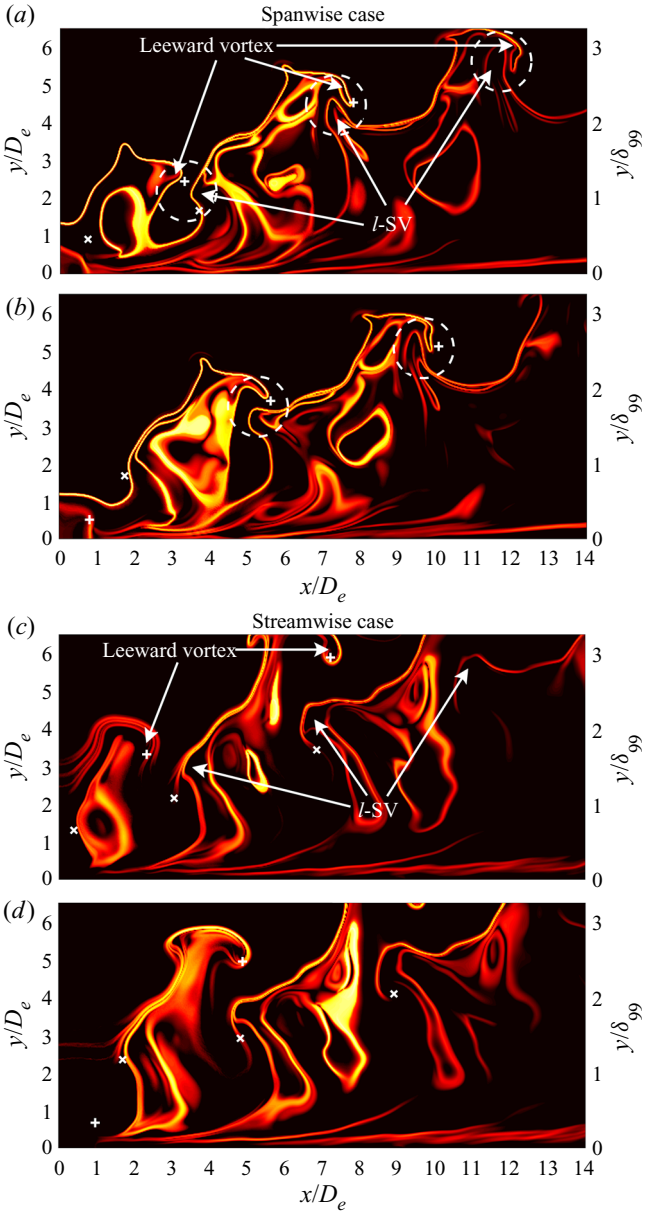


FIGURE 10. Contours of normalized backward-time FTLE in the jet symmetry plane at $t/T = 0.75$ (*a*,*c*) and 1.25 (*b*,*d*) for the (*a*,*b*) spanwise and (*c*,*d*) streamwise cases. The + and × denote vortex centre locations of the leeward vortex and the *l*-SV, respectively.

case can form a chain of TVRs connected by STVs due to the above vortex interactions, resulting in slower vortex penetration and recovery of the vortex ring tilting. The axis switching properties of the two cases can account for this difference. For the spanwise case, the vortex ring expands its diameter in the jet symmetry plane during the first axis switching (see figure 8*a*), which reduces the distance between the leeward vortex and the downstream *l*-SV, and triggers the subsequent vortex interaction. In contrast, the vortex

https://doi.org/10.1017/jfm.2020.430 Published online by Cambridge University Press

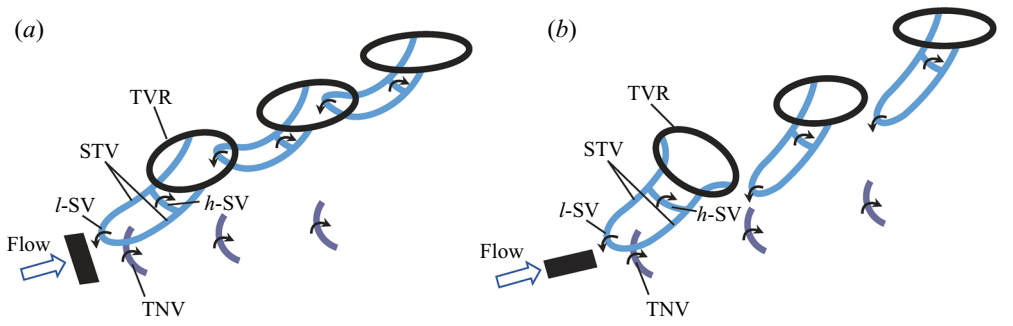


FIGURE 11. Schematic models of rectangular synthetic jets in cross-flow with (*a*) spanwise and (*b*) streamwise configurations. The black arrows denote the local rotation sense of vortical structures.

ring for the streamwise case shrinks its diameter in the jet symmetry plane during the first axis switching, and thus impedes the probable interaction.

A quantitative description of the vortex interaction effect is presented in figure 12. The formation of a counter-rotating vortex pair can weaken the strengths of the leeward vortex and the *l*-SV. Thus, the leeward vortex for the spanwise case displays an earlier decay of the circulation to a lower magnitude at around $x/D_e = 3$. Furthermore, the circulation of the *l*-SV cannot be detected after $x/D_e = 4$ for the spanwise case, while that is maintained to the downstream field for the streamwise case (figure 12*a*). Similar behaviour is also observed in the normalized power spectrum of the vertical velocity along the vortex-ring-centre trajectory (figure 12*b*). The normalization is performed to exhibit the relative variation of the dominant frequency peak more clearly. Compared to the streamwise case, the peaks of the dominant frequency and high-frequency harmonics for the spanwise case decrease more rapidly from $x/D_e = 0.5$ to 4 (see the black arrow locations), suggesting faster jet transition under vortex interactions. Note that these flow-field characteristics are essentially the results of axis switching of vortex rings, which can be conducive to enhancing jet mixing and heat transfer for the spanwise case. On the other hand, the trailing structures for the streamwise case have greater streamwise persistency. They in turn can induce larger upwash velocity, leading to a larger velocity deficit in the free stream, which will be demonstrated later.

5. Flow-field characteristics in cross-flow

5.1. *Mean flow field in the jet symmetry plane*

This section pays attention to the flow-field characteristics of rectangular synthetic jets in cross-flow, and discusses the impact of the orifice orientation on the downstream boundary layer. Figure 13(*a*) presents the time-averaged streamwise velocity profiles at different streamwise locations in the jet symmetry plane. The local contour of $\lambda_{ci}\omega_z/|\omega_z|$ for the spanwise case is provided in figure 13(*b*) to help understanding. A prominent velocity deficit can be observed in the near-field profiles, and the magnitude decreases with the jet uplifting. This velocity deficit is attributed to the upwash induced between the legs of the trailing structures, and inside the tilted vortex ring. In particular, the maximum velocity deficit of the spanwise case is lower than that of the streamwise case. That is associated with vortex interactions, which restrict persistency of the trailing structures, and weaken the vortex strength, as depicted in figure 12. However, this comparison is opposite to the

https://doi.org/10.1017/jfm.2020.430 Published online by Cambridge University Press

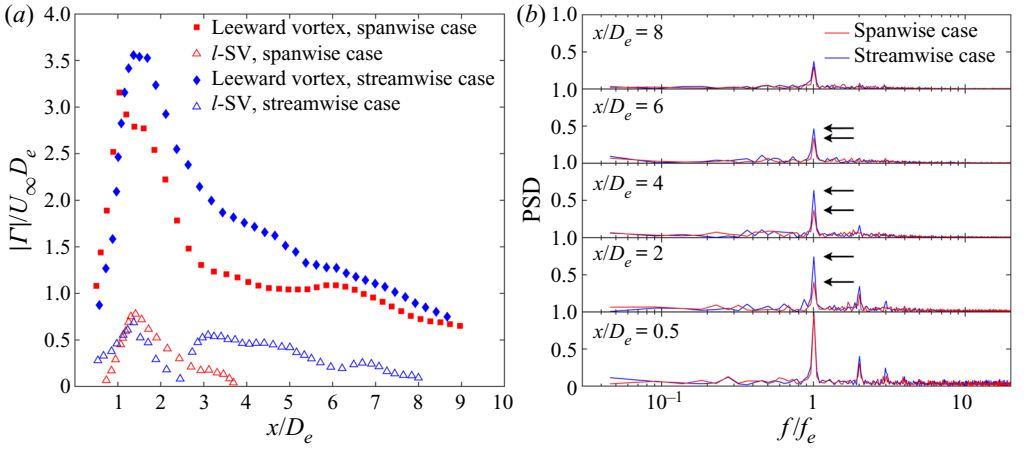


FIGURE 12. (*a*) Circulations of the leeward vortex and the *l*-SV, and (*b*) normalized PSD of vertical velocity U_y by the maximum along the vortex-ring-centre trajectory at $x/D_e = 0.5$, 2, 4, 6 and 8 for the two cases. The black arrows in (*b*) mark the peak locations of the dominant frequency.

previous results for steady jets (Gutmark, Ibrahim & Murugappan 2008) and higher-AR synthetic jets (Van Buren *et al.* 2016*b*) in cross-flow. The difference can be accounted for by no axis switching and following vortex interactions observed in those studies.

In addition, velocity overshoot appears on both sides of the velocity deficit region. The upper velocity overshoot results from local induced velocity upon the leeward vortex, while that inside the boundary layer after $x/D_e = 4$ is due to momentum transfer by the near-wall vortex. With the merging between the jet and the boundary layer, the velocity in the boundary-layer profile does not recover to the free-stream value. Hence, the current boundary-layer thickness cannot be determined by the traditional $99\,\%\,U_\infty$ criterion. According to the definition suggested by Sarkar & Sarkar (2009), we use the height of the local maximum of U_x between the wall and the velocity deficit region as the local boundary-layer thickness δ, as shown by the black dashed line at $x/D_e = 4$. Thus, the boundary-layer shape factor can be calculated as

$$H = \frac{\int_0^\delta \left(1 - \frac{U_x}{U_{x,max}}\right) \mathrm{d}y}{\int_0^\delta \frac{U_x}{U_{x,max}} \left(1 - \frac{U_x}{U_{x,max}}\right) \mathrm{d}y}, \tag{5.1}$$

where $U_{x,max}$ denotes the local maximum of U_x. The result in figure 13(*c*) indicates that the shape factor of the spanwise case is closer to the turbulent value ($H = 1.4$), corresponding to the larger velocity gradient inside the boundary layer.

The streamwise velocity fluctuation profiles in the jet symmetry plane are displayed in figure 14(*a*). The local peaks of velocity fluctuation in the jet region are caused by the tilted vortex ring and the shear-layer vortices. The corresponding maximum velocity fluctuation $u^{jet}_{rms,max}$ decreases with the jet uplifting (figure 14*b*). Since the spanwise case is more bent downstream by the cross-flow, it can produce slightly larger $u^{jet}_{rms,max}$ than the streamwise case before $x/D_e = 4$. However, as the trailing structures break down under vortex interactions, the spanwise case has a larger decay rate after $x/D_e = 5$.

https://doi.org/10.1017/jfm.2020.430 Published online by Cambridge University Press

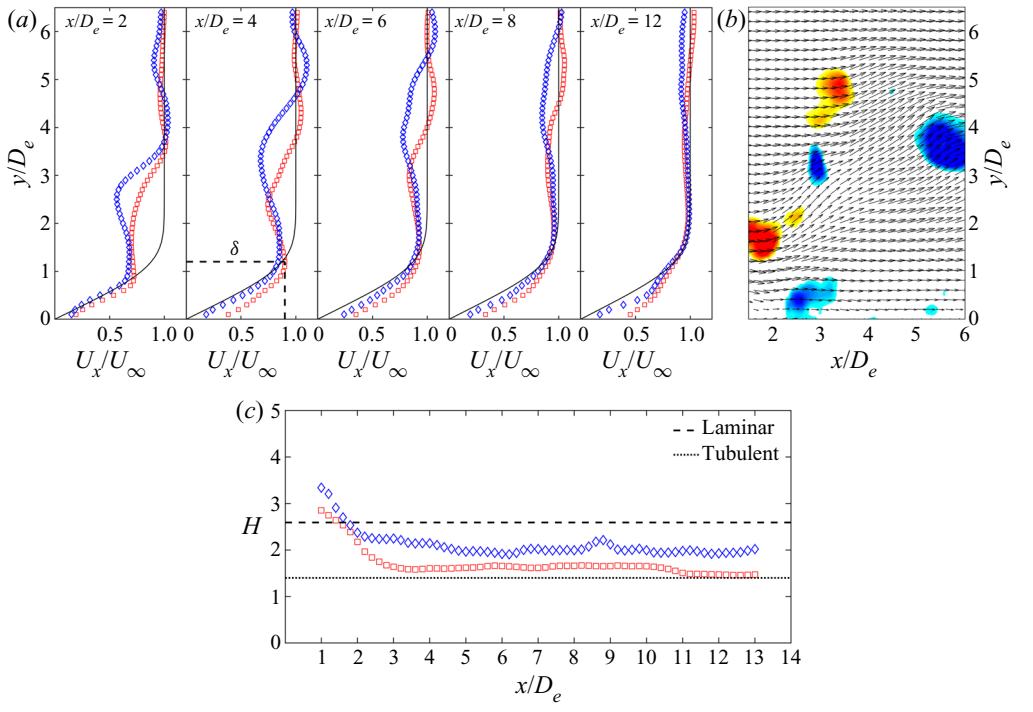


FIGURE 13. (*a*) Time-averaged streamwise velocity profile U_x/U_∞, (*b*) local contour of $\lambda_{ci}\omega_z/|\omega_z|$ ($\lambda_{ci} \geq 1.5$, $t/T = 0.25$ for the spanwise case) superposed by velocity vector, and (*c*) boundary-layer shape factor H in the jet symmetry plane, for □ (red), the spanwise case, and ◇ (blue), the streamwise case. The black solid line in (*a*) represents the Blasius profile, and the black dashed line at $x/D_e = 4$ denotes the definition for the boundary-layer thickness δ.

A new peak can be observed inside the boundary layer at around $y/D_e = 0.3$ (spanwise case) or 0.4 (streamwise case) downstream of $x/D_e = 4$ (figure 14*a*), which is contributed by the near-wall vortex. Following He, Wang & Pan (2013), an inflection point at the minimum of u_{rms} between the near-wall peak and the outside peak can be determined to define a sheltering edge δ_s, as shown by the black dashed line at $x/D_e = 4$. The sheltering edge is slightly smaller than δ, which can be used to exclude the jet's direct disturbance from the boundary layer in the later analysis. The spanwise case has a larger maximum velocity fluctuation inside the sheltering edge $u^{\delta_s}_{rms,max}$ than the streamwise case (figure 14*b*), close to the value of a canonical turbulent boundary layer (Spalart 1988). This result is perceived to stem from the larger upstream jet disturbance which is transferred into the boundary layer through the near-wall vortex.

5.2. *Mean flow field in the spanwise plane*

Figure 15(*a*,*c*) presents the spanwise distribution of the velocity deficit and overshoot $(U_{BL} - U_x)/U_\infty$ (here U_{BL} denotes the Blasius profile), superposed by the local time-averaged vorticity $|\bar{\omega}_{xyz}|D_e/U_\infty$ ($|\bar{\omega}_{xyz}| = \sqrt{\bar{\omega}_x^2 + \bar{\omega}_y^2 + \bar{\omega}_z^2}$). A positive value of $(U_{BL} - U_x)/U_\infty$ represents a velocity deficit and a negative value represents a velocity overshoot. Associated with weaker trailing structures and vortex ring (see $|\bar{\omega}_{xyz}|D_e/U_\infty$ in the jet region), the spanwise case exhibits lower peaks of the velocity deficit and overshoot

https://doi.org/10.1017/jfm.2020.430 Published online by Cambridge University Press

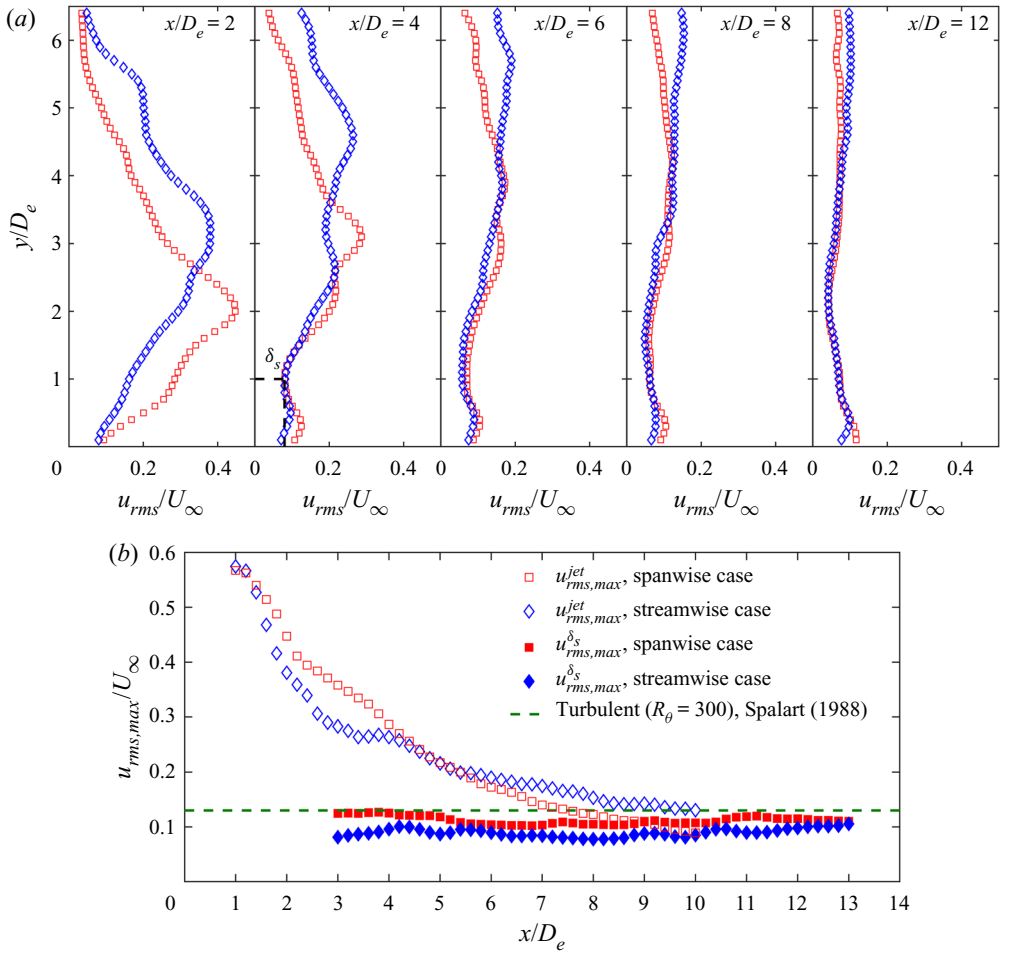


FIGURE 14. (*a*) Streamwise velocity fluctuation profile u_{rms}/U_∞, and (*b*) maximum velocity fluctuation in the jet region $u^{jet}_{rms,max}$, and the sheltering edge $u^{\delta_s}_{rms,max}$ in the jet symmetry plane, for □ (red), the spanwise case, and ◇ (blue), the streamwise case. The black dashed line at $x/D_e = 4$ in (*a*) denotes the definition for the sheltering edge δ_s.

than the streamwise case in the jet region. In contrast, the peak of the velocity overshoot inside the boundary layer is larger for the spanwise case.

The spanwise distribution of the streamwise velocity fluctuation is shown in figure 15(*b*,*d*). Owing to slower vortex penetration, the impact of the jet disturbance on the boundary layer can persist more downstream for the spanwise case. For instance, the disturbance of $u_{rms}/U_\infty = 0.05$ is jointed between the jet and the boundary layer at $x/D_e = 8$ for the spanwise case; however, that has been completely separated by the local sheltering edge for the streamwise case. Accordingly, the spanwise case has larger velocity fluctuation peak inside the boundary layer, displaying the merit of promoting boundary-layer transition.

Using (5.1), the spatial distribution of the boundary-layer shape factor is given in figure 16. Overall, the boundary-layer shape factors for the two cases decrease in the streamwise direction, reflecting the trend of boundary-layer transition to a turbulent one.

https://doi.org/10.1017/jfm.2020.430 Published online by Cambridge University Press

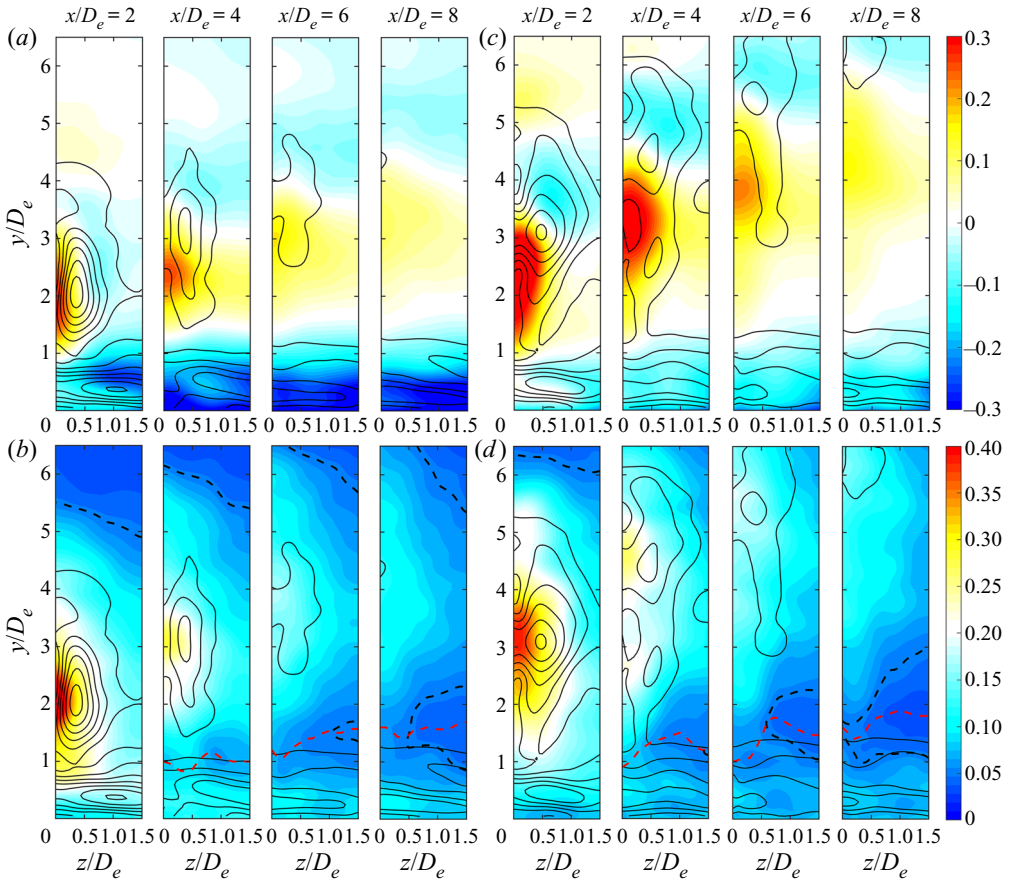


FIGURE 15. Spanwise distributions of (*a*,*c*) velocity deficit and overshoot $(U_{BL} - U_x)/U_\infty$, and (*b*,*d*) streamwise velocity fluctuation u_{rms}/U_∞ for the (*a*,*b*) spanwise and (*c*,*d*) streamwise cases. The black solid line denotes the time-averaged vorticity $|\bar{\omega}_{xyz}|D_e/U_\infty$ with minimum value of 0.2 and interval of 0.2; the black dashed line in (*b*,*d*) denotes the contour of $u_{rms}/U_\infty = 0.05$; and the red dashed line denotes the sheltering edge δ_s.

In particular, the global shape factor of the spanwise case is lower than that of the streamwise case, consistent with the characteristics of larger velocity gradient and velocity fluctuation peak inside the boundary layer. This suggests that the spanwise orifice orientation could be more efficient to energize the boundary layer for resisting streamwise adverse pressure gradients.

5.3. *Disturbance development inside boundary layer*

Based on the above analysis, the boundary-layer transition in the lee side of the jet is associated with the near-wall vortex induced by synthetic jets. To further reveal the disturbance impact of the near-wall vortex on the boundary layer, the FMD method is used to extract the relevant dynamical information. The flow field in the range of $[1, 14]D_e \times [0, 4]D_e \times [-1.5, 1.5]D_e$ in three directions is selected to perform the FMD, which contains the entire boundary-layer region downstream of the jet.

https://doi.org/10.1017/jfm.2020.430 Published online by Cambridge University Press

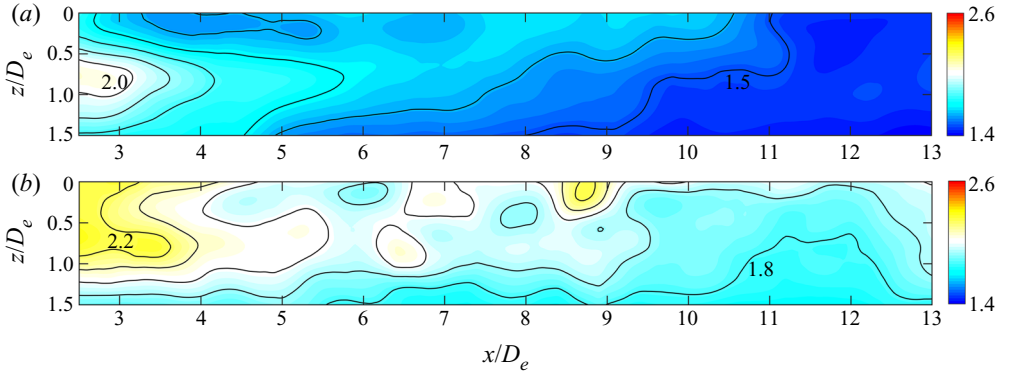


FIGURE 16. Spatial distribution of boundary-layer shape factor H for the (a) spanwise and (b) streamwise cases. Contour levels are 0.1.

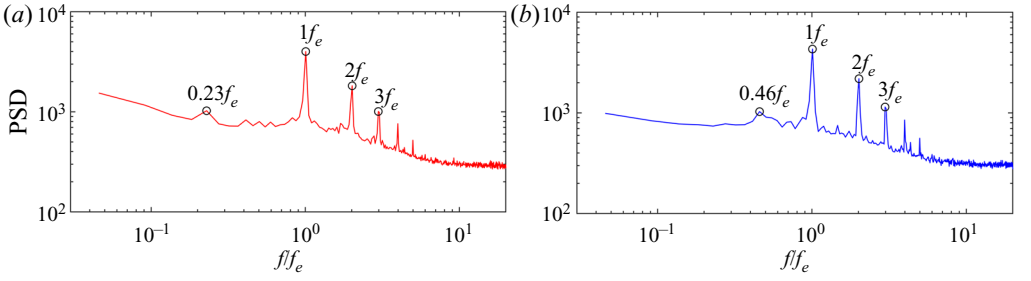


FIGURE 17. Global FMD spectrum of the selected region for the (a) spanwise and (b) streamwise cases.

Figure 17 presents the global FMD power spectrum of the selected flow field for the three velocity components at each sampling point. The power spectra of the two cases both display profound peaks corresponding to the excitation frequency and its high-frequency harmonics. In addition, the peaks at lower frequencies of $0.23f_e$ for the spanwise case, and $0.46f_e$ for the streamwise case, can be detected corresponding to the low-frequency disturbance components.

The spatial FMD modes with the marked characteristic frequencies are examined, and figure 18 shows the streamwise components of these modes in the jet symmetry plane. Only the imaginary part of each spatial mode is given due to the conjugate relation between the real and imaginary parts. The modes upon the boundary layer reveal the jet structures with different spatial scales. The streamwise wavelength of these structures decreases with increased frequency. Inside the boundary layer, the near-wall modes with the dominant frequency of $1.0f_e$ characterize the downstream convection of the near-wall vortex (figure 18b,f).

At a lower frequency of $0.23f_e$, it is noted that an elongated structure with considerably large spatial scale appears at the downstream location for the spanwise case (figure 18a), similar to the result of boundary-layer transition induced by a circular cylinder wake in He *et al.* (2013). This suggests that the low-frequency disturbance of $0.23f_e$ can persist downstream independent of the external excitation frequency. In fact, similar structures with different spatial scales can also be found in some other low-frequency modes. For the streamwise case, the elongated structures are weaker (figure 18e), probably due to the

https://doi.org/10.1017/jfm.2020.430 Published online by Cambridge University Press

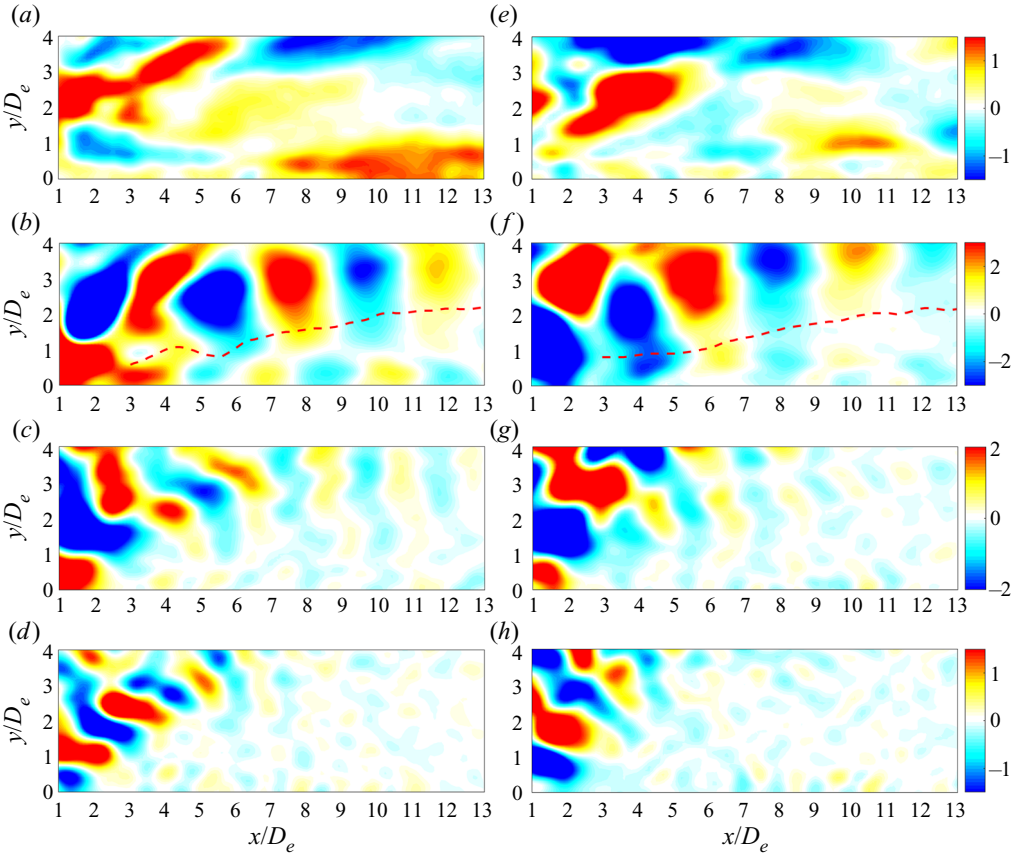


FIGURE 18. Streamwise components of FMD modes in the jet symmetry plane with different frequencies for the two cases: (*a*) $0.23f_e$, (*b*) $1.0f_e$, (*c*) $2.0f_e$ and (*d*) $3.0f_e$ for the spanwise case; (*e*) $0.46f_e$, (*f*) $1.0f_e$, (*g*) $2.0f_e$ and (*h*) $3.0f_e$ for the streamwise case. The red dashed line in (*b*,*f*) denotes the sheltering edge.

relatively lower disturbance amplitude, which will be presented in figure 19. At higher frequencies of $2.0f_e$ and $3.0f_e$, no near-wall modes with comparable amplitude relative to those in the jet region are observed.

To quantitatively measure the disturbance amplitude of different frequencies, we compute the averaged boundary-layer disturbance energy E_{uu}^{fi} with a frequency f_i as

$$E_{uu}^{fi} = \int\int_0^{\delta_s} (u_{rms}^{fi})^2 \,\mathrm{d}y\,\mathrm{d}z \Big/ \int\int_0^{\delta_s} U_\infty^2 \,\mathrm{d}y\,\mathrm{d}z, \tag{5.2}$$

where u_{rms}^{fi} represents the streamwise velocity fluctuation of the flow field with the frequency f_i. Note that the integral upper limit here is selected as δ_s instead of δ to exclude the direct contribution of the jet disturbance. The boundary-layer disturbance energies of the selected frequencies ($0.23f_e$, $0.46f_e$, $1.0f_e$ and $2.0f_e$) for the two cases are compared in figure 19(*b*), and the vorticity peak of the near-wall vortex is given in figure 19(*a*) to aid interpretation.

As shown in figure 19(*b*), compared to the streamwise case, the disturbance energy of $1.0f_e$ for the spanwise case has significantly larger initial magnitude followed by a

https://doi.org/10.1017/jfm.2020.430 Published online by Cambridge University Press

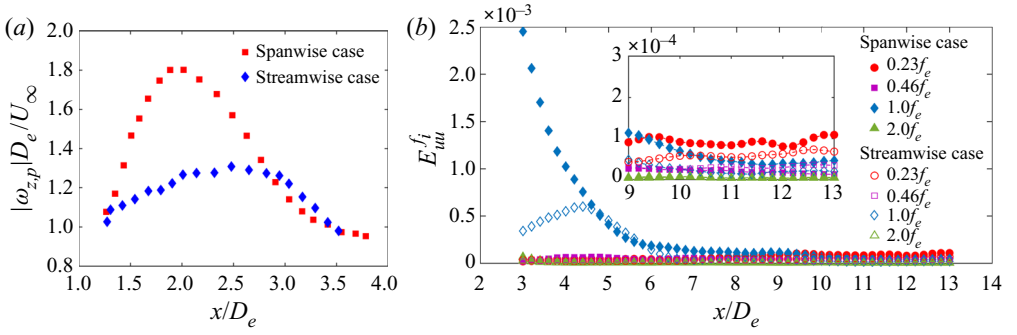


FIGURE 19. Streamwise evolution of (*a*) vorticity peak $|\omega_{z,p}|D_e/U_\infty$ of the near-wall vortex, and (*b*) averaged boundary-layer disturbance energy $E_{uu}^{f_i}$ of the FMD modes with different frequencies f_i for the two cases.

faster decay in the near flow field ($x/D_e < 6$). This result is ascribed to the stronger near-wall vortex for the spanwise case (figure 19*a*), which yields larger initial disturbance to trigger boundary-layer transition. Additionally, the short growth stage of $1.0f_e$ for the streamwise case could be related to the more downstream vorticity peak of the near-wall vortex. Since the current boundary-layer flow is in the early stage of the transition, the disturbance energies of the low-frequency components grow at a much slow rate. Even so, the magnitude of $1.0f_e$ has decayed to be lower than that of $0.23f_e$ after approximately $x/D_e = 9.3$ for the two cases. Particularly, $0.23f_e$ for the spanwise case has the largest disturbance magnitude corresponding to more turbulent characteristics. Such a result can help to understand the mechanism of boundary-layer transition induced by synthetic jets.

6. Conclusions

In this paper, we experimentally investigate the 3-D flow fields of an AR = 3 rectangular synthetic jet and its interaction with a laminar cross-flow using time-resolved tomographic PIV. Two typical orifice orientations, spanwise and streamwise configurations, are concerned to analyse the vortical evolution and the relevant flow physics.

Compared to the quiescent condition, the vortical structures for rectangular synthetic jets in cross-flow are more complicated, which are composed of a tilted vortex ring (TVR), a secondary trailing vortex (STV) and a tertiary near-wall vortex (TNV). The flow scenarios are evidently different from those for high-AR (AR > 5) cases (Van Buren *et al.* 2016*a*,*b*). Also, some differences are found compared with the tilted and distorted vortex rings for circular cases (Jabbal & Zhong 2010): the legs of the present STV are jointed in the spanwise direction by two shear-layer vortices at different wall-normal heights, named *l*-SV and *h*-SV; the present TNV is a crescent-shaped spanwise vortex instead of a streamwise vortex pair as in Jabbal & Zhong (2010).

For the first time, as the peculiar property of non-circular vortex rings in quiescent condition, axis switching is detected for low-AR rectangular synthetic jets in cross-flow. The orifice orientation has a direct impact on the time and location of axis switching. Furthermore, axis switching can cause vortex interaction for the spanwise case, where the leeward vortex of the TVR and the downstream *l*-SV become a pair of contour-rotating vortices. As a result, the spanwise case forms a chain of TVRs connected by the STVs; however, they are relatively independent for the streamwise case. Under vortex

https://doi.org/10.1017/jfm.2020.430 Published online by Cambridge University Press

interactions, the spanwise case yields slower recovery of the vortex ring tilting and penetration through the boundary layer, but faster jet transition.

The time-averaged flow fields in the jet symmetry and spanwise planes are examined, respectively. Owing to weaker trailing structures and vortex ring, the spanwise case exhibits lower peaks of the velocity deficit and overshoot in the jet region. In contrast, inside the boundary layer, the spanwise case produces larger velocity gradient and velocity fluctuation peak based on momentum transfer from the outer flow, leading to a lower global boundary-layer shape factor than the streamwise case. These suggest that the spanwise orientation is more efficient in energizing the boundary layer. Further the FMD method is applied to extract important dynamical information from the boundary layer. The results indicate that the spanwise case produces significantly larger initial disturbance of $1.0f_e$ with a larger near-field decay rate than the streamwise case through inducing a stronger near-wall vortex. In addition, the disturbance energy of the low-frequency component $0.23f_e$ can persist downstream, which exceeds that of $1.0f_e$ after approximately $x/D_e = 9.3$ for the two cases. Particularly, $0.23f_e$ of the spanwise case has the largest magnitude corresponding to faster boundary-layer transition characteristics.

It is necessary to discuss how the current results can benefit the flow control community. First, this paper has characterized the 3-D flow structures in detail. The scenarios are generated in a simplified flow; however, they may be applied to the situation with more complex flows, such as a turbulent boundary layer or flow separation on an airfoil according to previous research (Zhong *et al.* 2005; Van Buren *et al.* 2016*a*). Second, understanding the mechanism of fundamental interactions of low-AR rectangular synthetic jets with a cross-flow is crucial for their practical applications. This paper has revealed the mechanism involving two aspects: the interaction with the outer flow related to axis switching of vortex rings, and the influence on the boundary layer by the near-wall vortex. These provide a possible path to improve flow control effectiveness, e.g. increased jet mixing or faster boundary-layer transition to turbulence, through changing the axis switching characteristics or the strength of the vortex. However, the present work is the first step, and more investigations on the influence of other parameters and practical applications of low-AR non-circular synthetic jets should be conducted step by step to obtain a full range of flow control implementation.

Acknowledgements

This work was supported by the National Natural Science Foundation of China (nos. 11722215 and 11721202).

Declaration of interests

The authors report no conflict of interest.

REFERENCES

AMITAY, M. & CANNELLE, F. 2006 Evolution of finite span synthetic jets. *Phys. Fluids* **18** (5), 054101.

CANTWELL, B. & COLES, D. 1983 An experimental study of entrainment and transport in the turbulent near wake of a circular cylinder. *J. Fluid Mech.* **136**, 321–374.

CATER, J. E. & SORIA, J. 2002 The evolution of round zero-net-mass-flux jets. *J. Fluid Mech.* **472**, 167–200.

CROOK, A. & WOOD, N. J. 2001 Measurements and visualization of synthetic jets. *AIAA Paper* 2001–0145. American Institute of Aeronautics and Astronautics.

https://doi.org/10.1017/jfm.2020.430 Published online by Cambridge University Press

DANDOIS, J., GARNIER, E. & SAGAUT, P. 2007 Numerical simulation of active separation control by a synthetic jet. *J. Fluid Mech.* **574**, 25–58.

DEMAURO, E. P., LEONG, C. M. & AMITAY, M. 2013 Interaction of a synthetic jet with the flow over a low aspect ratio cylinder. *Phys. Fluids* **25** (6), 064104.

ELSINGA, G. E., SCARANO, F., WIENEKE, B. & VAN OUDHEUSDEN, B. W. 2006 Tomographic particle image velocimetry. *Exp. Fluids* **41** (6), 933–947.

FENG, L. H., & WANG, J. J. 2010 Circular cylinder vortex-synchronization control with a synthetic jet positioned at the rear stagnation point. *J. Fluid Mech.* **662**, 232–259.

FENG, L. H. & WANG, J. J. 2014 The virtual aeroshaping enhancement by synthetic jets with variable suction and blowing cycles. *Phys. Fluids* **26** (1), 014105.

FRIC, T. F. & ROSHKO, A. 1994 Vortical structure in the wake of a transverse jet. *J. Fluid Mech.* **279**, 1–47.

GLEZER, A. & AMITAY, M. 2002 Synthetic jets. *Ann. Rev. Fluid Mech.* **34**, 503–529.

GREEN, M. A., ROWLEY, C. W. & HALLER, G. 2007 Detection of Lagrangian coherent structures in three-dimensional turbulence. *J. Fluid Mech.* **572**, 111–120.

GRINSTEIN, F. F. 2001 Vortex dynamics and entrainment in rectangular free jets. *J. Fluid Mech.* **437**, 69–101.

GUTMARK, E. J. & GRINSTEIN, F. F. 1999 Flow control with noncircular jets. *Ann. Rev. Fluid Mech.* **31**, 239–272.

GUTMARK, E. J., IBRAHIM, I. M. & MURUGAPPAN, S. 2008 Circular and noncircular subsonic jets in cross flow. *Phys. Fluids* **20** (7), 075110.

HALLER, G. 2015 Lagrangian coherent structures. *Ann. Rev. Fluid Mech.* **47**, 137–161.

HALLER, G. & YUAN, G. 2000 Lagrangian coherent structures and mixing in two-dimensional turbulence. *Physica* D **147** (3–4), 352–370.

HE, G. S., WANG, J. J. & PAN, C. 2013 Initial growth of a disturbance in a boundary layer influenced by a circular cylinder wake. *J. Fluid Mech.* **718**, 116–130.

HOLMAN, R., UTTURKAR, Y., MITTAL, R., SMITH, B. & CATTAFESTA, L. 2005 Formation criterion for synthetic jets. *AIAA J.* **43** (10), 2110–2115.

JABBAL, M. & ZHONG, S. 2008 The near wall effect of synthetic jets in a boundary layer. *Intl J. Heat Fluid Flow* **29** (1), 119–130.

JABBAL, M. & ZHONG, S. 2010 Particle image velocimetry measurements of the interaction of synthetic jets with a zero-pressure gradient laminar boundary layer. *Phys. Fluids* **22** (6), 063603.

KELSO, R. M., LIM, T. T. & PERRY, A. E. 1996 An experimental study of round jets in cross-flow. *J. Fluid Mech.* **306**, 111–144.

KOTAPATI, R. B., MITTAL, R. & CATTAFESTA, L. N. III 2007 Numerical study of a transitional synthetic jet in quiescent external flow. *J. Fluid Mech.* **581**, 287–321.

LARDEAU, S. & LESCHZINER, M. A. 2011 The interaction of round synthetic jets with a turbulent boundary layer separating from a round ramp. *J. Fluid Mech.* **683**, 172–211.

LIM, T. T., NEW, T. H. & LUO, S. C. 2001 On the development of large-scale structures of a jet normal to a cross flow. *Phys. Fluids* **13** (3), 770–775.

MA, L. Q., FENG, L. H., PAN, C., GAO, Q. & WANG, J. J. 2015 Fourier mode decomposition of PIV data. *Sci. China Technol. Sci.* **58** (11), 1935–1948.

MAHESH, K. 2013 The interaction of jets with crossflow. *Ann. Rev. Fluid Mech.* **45**, 379–407.

MARGASON, R. J. 1993 Fifty years of jet in cross flow research. *AGARD Paper* CP-534. AGARD.

NEW, T. H., LIM, T. T. & LUO, S. C. 2003 Elliptic jets in cross-flow. *J. Fluid Mech.* **494**, 119–140.

NICHOLS, J. W., SCHMID, P. J. & RILEY, J. J. 2007 Self-sustained oscillations in variable-density round jets. *J. Fluid Mech.* **29**, 285–326.

QU, Y., WANG, J. J., SUN, M., FENG, L. H., PAN, C., GAO, Q. & HE, G. S. 2017 Wake vortex evolution of square cylinder with a slot synthetic jet positioned at the rear surface. *J. Fluid Mech.* **812**, 940–965.

RAVI, B. R., MITTAL, R. & NAJJAR, F. M. 2004 Study of three-dimensional synthetic jet flowfields using direct numerical simulation. *AIAA Paper* 2004–0091. American Institute of Aeronautics and Astronautics.

SARKAR, S. & SARKAR, S. 2009 Large-eddy simulation of wake and boundary layer interactions behind a circular cylinder. *Trans. ASME: J. Fluids Engng* **131** (9), 091201.

https://doi.org/10.1017/jfm.2020.430 Published online by Cambridge University Press

SAU, R. & MAHESH, K. 2008 Dynamics and mixing of vortex rings in crossflow. *J. Fluid Mech.* **604**, 389–409.

SCARANO, F. & RIETHMULLER, M. L. 2000 Advances in iterative multigrid PIV image processing. *Exp. Fluids* **29** (1), S051–S060.

SHADDEN, S. C., DABIRI, J. O. & MARSDEN, J. E. 2006 Lagrangian analysis of fluid transport in empirical vortex ring flows. *Phys. Fluids* **18** (4), 047105.

SHI, X. D., FENG, L. H. & WANG, J. J. 2019 Evolution of elliptic synthetic jets at low Reynolds number. *J. Fluid Mech.* **868**, 66–96.

SMITH, D. R. 2002 Interaction of a synthetic jet with a crossflow boundary layer. *AIAA J.* **40** (11), 2277–2288.

SMITH, B. L. & GLEZER, A. 1998 The formation and evolution of synthetic jets. *Phys. Fluids* **10** (9), 2281–2297.

SMITH, S. H. & MUNGAL, M. G. 1998 Mixing, structure and scaling of the jet in crossflow. *J. Fluid Mech.* **357**, 83–122.

SMITH, B. L. & SWIFT, G. W. 2003 A comparison between synthetic jets and continuous jets. *Exp. Fluids* **34** (4), 467–472.

SPALART, P. R. 1988 Direct simulation of a turbulent boundary layer up to $R_\theta = 1410$. *J. Fluid Mech.* **187**, 61–98.

TANG, H., SALUNKHE, P., ZHENG, Y. Y., DU, J. X. & WU, Y. H. 2014 On the use of synthetic jet actuator arrays for active flow separation control. *Exp. Therm. Fluid Sci.* **57**, 1–10.

VAN BUREN, T. & AMITAY, M. 2016 Comparison between finite-span steady and synthetic jets issued into a quiescent fluid. *Exp. Therm. Fluid Sci.* **75**, 16–24.

VAN BUREN, T., BEYAR, M., LEONG, C. M. & AMITAY, M. 2016*a* Three-dimensional interaction of a finite-span synthetic jet in a crossflow. *Phys. Fluids* **28** (3), 037105.

VAN BUREN, T., BEYAR, M., LEONG, C. M. & AMITAY, M. 2016*b* Impact of orifice orientation on a finite-span synthetic jet interaction with a crossflow. *Phys. Fluids* **28** (3), 037106.

VAN BUREN, T., WHALEN, E. & AMITAY, M. 2014 Vortex formation of a finite-span synthetic jet: effect of rectangular orifice geometry. *J. Fluid Mech.* **745**, 180–207.

WANG, L., FENG, L. H., WANG, J. J. & LI, T. 2018 Evolution of low-aspect-ratio rectangular synthetic jets in a quiescent environment. *Exp. Fluids* **59** (6), 91.

WANG, L., FENG, L. H. & XU, Y. 2019 Laminar-to-transitional evolution of three-dimensional vortical structures in a low-aspect-ratio rectangular synthetic jet. *Exp. Therm. Fluid Sci.* **104**, 129–140.

WANG, C. Y., GAO, Q., WANG, H. P., WEI, R. J. & WANG, J. J. 2016 Divergence-free smoothing for volumetric PIV data. *Exp. Fluids* **57** (1), 1–23.

WIENEKE, B. 2008 Volume self-calibration for 3D particle image velocimetry. *Exp. Fluids* **45** (4), 549–556.

XU, Y., WANG, J. J., FENG, L. H., HE, G. S. & WANG, Z. Y. 2018 Laminar vortex ring impinging onto porous walls with a constant porosity. *J. Fluid Mech.* **837**, 729–764.

YE, Q. Q., SCHRIJER, F. F. & SCARANO, F. 2016 Boundary layer transition mechanism behind a micro-ramp. *J. Fluid Mech.* **793**, 132–161.

ZHANG, S. & ZHONG, S. 2011 Turbulent flow separation control over a two-dimensional ramp using synthetic jets. *AIAA J.* **49** (12), 2637–2649.

ZHONG, S., MILLET, F. & WOOD, N. J. 2005 The behavior of circular synthetic jets in a laminar boundary layer. *Aeronaut. J.* **109** (1100), 461–470.

ZHOU, J., ADRIAN, R. J., BALACHANDAR, S. & KENDALL, T. M. 1999 Mechanisms for generating coherent packets of hairpin vortices in channel flow. *J. Fluid Mech.* **387**, 353–396.

ZHOU, J. & ZHONG, S. 2009 Numerical simulation of the interaction of a circular synthetic jet with a boundary layer. *Comput. Fluids* **38** (2), 393–405.

ZHOU, J. & ZHONG, S. 2010 Coherent structures produced by the interaction between synthetic jets and a laminar boundary layer and their surface shear stress patterns. *Comput. Fluids* **39** (8), 1296–1313.

ZHU, H. Y., WANG, C. Y., WANG, H. P. & WANG, J. J. 2017 Tomographic PIV investigation on 3D wake structures for flow over a wall-mounted short cylinder. *J. Fluid Mech.* **831**, 743–778.

ZONG, H. & KOTSONIS, M. 2019 Effect of velocity ratio on the interaction between plasma synthetic jets and turbulent cross-flow. *J. Fluid Mech.* **856**, 928–962.

https://doi.org/10.1017/jfm.2020.430 Published online by Cambridge University Press